



ELSEVIER

Physica D 2889 (2002) 1–35

---



---

**PHYSICA D**


---



---

www.elsevier.com/locate/physd

3                    **Baroclinic and barotropic aspects of the wind-driven**  
 4                    **ocean circulation**<sup>☆</sup>

5                    M. Ghil<sup>\*</sup>, Y. Feliks<sup>2</sup>, L.U. Sushama

6                    *Department of Atmospheric Sciences and Institute of Geophysics and Planetary Physics,*  
 7                    *University of California, Los Angeles, CA 90095-1565, USA*

8                    Received 23 July 2001; received in revised form 5 February 2002

9                    Communicated by R. Temam

---

10 **Abstract**

11     The double-gyre circulation induced by a symmetric wind-stress pattern in a quasi-geostrophic model of the mid-latitude  
 12     ocean is studied analytically and numerically. The model is discretized vertically by projection onto normal modes of the  
 13     mean stratification. Within its horizontally rectangular domain, the numerical model captures the wind-driven circulation's  
 14     three dynamic regimes: (1) a basin-scale double-gyre circulation, cyclonic in the basin's northern part and anticyclonic in the  
 15     south, which is dominated by Sverdrup balance; (2) a swift western boundary current in either gyre, with dissipation most  
 16     important near the coast and inertial balance further out; and (3) a strong recirculating dipole near the intersection of the  
 17     western boundary with the symmetry line of zero wind-stress curl. The flow inside this stationary dipole is highly nonlinear,  
 18     and equivalent-barotropic. An analytical solution to the potential vorticity equation with variable stratification describes the  
 19     dipole, and fits well the full numerical model's steady-state solutions.

20     Changes in the numerical model's solutions are investigated systematically as a function of changes in the strength of  
 21     the wind stress  $\tau$  and the Rossby radius of deformation  $L_R$ . The main changes occur in the recirculation region, while the  
 22     basin-scale gyres and the western boundary currents are affected but little. A unique symmetric dipole is observed for small  $\tau$ ,  
 23     and agrees in its properties with the analytical solution. As  $\tau$  increases, multiple asymmetric equilibria arise due to pitchfork  
 24     bifurcation and are stable for large enough  $L_R$ . The numerically obtained asymmetric equilibria also agree in their main  
 25     properties with the analytical ones, as well as with the corresponding solutions of a shallow-water model.

26     Increasing  $\tau$  further results in two successive Hopf bifurcations, that lead to limit cycles with periods near 10 and 1 years,  
 27     respectively. Both oscillatory instabilities have a strong baroclinic component. Above a certain threshold in  $\tau$  the solutions  
 28     become chaotic. Flow pattern evolution in this chaotic regime resembles qualitatively the circulation found in the Gulf Stream  
 29     and Kuroshio current systems after their separation from the continent. © 2002 Elsevier Science B.V. All rights reserved.

30     PACS: 92.10.-c; 47.20.Ky; 05.45.Jn; 05.45.Yv

31     *Keywords:* Geophysical flows; Ocean circulation; Symmetry breaking; Successive bifurcations; Localized coherent structures

---

☆ Preliminary results of this investigation were presented as part of an invited talk by MG at the Newton Institute's EuroConference on Ocean Dynamics, 9–13 September 1996, Cambridge, UK.

\* Corresponding author. Tel.: +1-310-206-2285; fax: +1-310-206-3051/5219.

E-mail address: mghil@atmos.ucla.edu (M. Ghil).

<sup>1</sup> Permanent address: Department of Mathematics, Israel Institute of Biological Research, Ness-Ziona 70450, Israel.

## 1. Introduction and motivation

The large-scale flow of the mid-latitude oceans is dominated by the presence of a larger, anticyclonic and a smaller, cyclonic gyre. They are induced by the shear in the near-surface winds that cross the respective ocean basins: eastward in mid-latitudes and westward in low, tropical and high, polar latitudes. The two gyres share the eastward extension of western boundary currents, such as the Gulf Stream or Kuroshio. The oceanic boundary currents and eastward jets carry substantial amounts of heat and momentum; the jets also contribute to mixing in the oceans by their “whiplashing” oscillations and the detachment of eddies from them.

The mid-latitude ocean basins’ double-gyre wind-driven circulation is therefore a major research area in physical oceanography [1–7]. Recent interest in the climate’s interannual and interdecadal variability [8,9] has stimulated research into a new aspect of this classical problem. Jiang et al. [10,11] (the latter to be referred to as JJG hereafter) showed, in a simple shallow-water model, that interannual variability can arise in the double-gyre circulation in the presence of wind stress that is constant in time. An extensive review of earlier relevant work, observational and theoretical, can be found in JJG and in [7]. We update these reviews here briefly and emphasize the broader fluid-dynamical context.

Cessi and Ierley [12] found multiple equilibria (up to seven) in their barotropic quasi-geostrophic (QG) model; in geophysical fluid dynamics [6,13] barotropic refers to single-layer, homogeneous-density models, while quasi-geostrophy refers to the dominant balance between the pressure gradient and the Coriolis force. Antisymmetric, as well as asymmetric steady solutions were found in [12]. Some of these solutions fill the whole basin, while others decay rapidly to zero away from the western shore of the ocean basin.

Jiang et al. [10], JJG, and Speich et al. [14] studied this problem with a reduced-gravity shallow-water model, in which an active fluid layer of finite depth overlies an inert layer of infinite depth. They found multiple equilibria and, more importantly, periodic and chaotic solutions for different, fairly realistic parameter regimes, when increasing the wind stress  $\tau$  or decreasing the lateral diffusivity  $A_H$ . The periodic solutions they found were of two types, with periods of several years and several weeks, respectively. The interannual periods survived as broadened spectral peaks in the chaotic regime (JJG) and compared favorably with those found in observed time series of the Gulf Stream and Kuroshio axis [14].

McCalpin and Haidvogel [15] investigated the behavior of a reduced-gravity QG model, but found no steady-state solutions for the problem, although they used the same wind stress and bottom friction as JJG and Speich et al. did. The difference in results is probably due to the fact that McCalpin and Haidvogel applied a free-slip boundary condition at the lateral boundaries, while the former authors used basically a no-slip boundary condition.

JJG showed (see their Appendix A and further references there) that one can consider a generalized, partial-slip boundary condition that depends on a parameter  $\gamma$ : as  $\gamma$  increases from 0 to 1, free-slip becomes no-slip. Partial slip is, in fact, a more realistic boundary condition for simple, idealized models of this type, since the flow velocity in the ocean goes to zero at the boundary over spatial scales that are not resolved by these models and thus involve unresolved variations in depth of the basin. Increasing  $\gamma$  has a similar effect on the solutions as decreasing  $\tau$  or increasing  $A_H$ . Thus, Cessi and Ierley [12] found a steady state while using a free-slip boundary condition only when horizontal diffusion was several orders of magnitude larger than that used by JJG and Speich et al. [14]; see also [16,17].

Dijkstra and Katsman [18] examined the bifurcation diagram of the double-gyre problem as a function of lateral diffusion—measured by the inverse of a Reynolds number  $Re$ —for two versions of a QG model: one similar to McCalpin and Haidvogel’s, with an upper active and a lower inert layer, the other with two active layers. In the basic state of both model versions, the flow in the lower layer was motionless. Thus the main difference between the two versions is that genuine baroclinic motions, with energy conversion between lateral shear and vertical stratification [6,13], can occur only in the 2-layer one. The two types of wind-driven motions—barotropic and baroclinic—are sufficiently different from each other to warrant two separate chapters in Pedlosky’s book [7].

76 The bifurcation curves of Dijkstra and Katsman’s two model versions differ qualitatively in that there are no stable  
77 asymmetric steady states in the 2-layer version, while they do exist in the “1.5-layer”, reduced-gravity version. This  
78 difference can be explained mathematically as follows: in the 1.5-layer version, the first Hopf bifurcation occurs  
79 for larger  $Re$  (smaller diffusion) than the symmetry breaking due to pitchfork bifurcation. In the 2-layer version,  
80 however, Hopf bifurcation occurs already for smaller  $Re$  (larger diffusion), at which the (anti)symmetric branch is  
81 still stable, while the symmetry breaking due to pitchfork bifurcation occurs at larger  $Re$ . Dijkstra and Katsman’s  
82 study was carried out at a Rossby radius of deformation of  $L_R = 30$  km; the deformation radius characterizes the  
83 horizontal extent of the most energetic motions in a rotating fluid. We shall see that, for larger values of  $L_R$ , the  
84 conclusion of Dijkstra and Katsman [18] does not hold. Our study of solution dependence will thus shed further  
85 light on the physical reasons for the above-noted difference between the ordering of instabilities in a 1.5-layer and  
86 2-layer QG model.

87 In Dijkstra and Katsman’s 2-layer model [18] two Hopf bifurcations were obtained: the first one, at smaller  
88  $Re$ , leads to a limit cycle with a period of 11 months, the second one, at larger  $Re$ , has a period of 1.5 years. The  
89 perturbation in the lower layer leads to the one in the upper layer by approximately 1/4 period. This vertical structure  
90 of the destabilizing perturbation demonstrates the baroclinic nature of the instability and adds weight to our interest  
91 in the relative role of baroclinic and barotropic contributions to the ocean’s low-frequency variability.

92 Berloff and Meacham [19,20] examined the circulation in a small rectangular basin driven by wind forcing that  
93 gives rise to a single gyre (see also Section 2.14 of [7]). They used a barotropic and a baroclinic QG model and studied  
94 the role of the horizontal diffusion as a control parameter. Their low-frequency circulation has low-dimensional  
95 behavior in phase space and is dominated by two flow patterns in physical space: (i) a single basin-scale gyre with  
96 a strong peripheral current; and (ii) a set of recirculating gyres, from one to three, in the southwestern part of the  
97 basin. These two flow patterns are similar in both the barotropic and baroclinic models. The most common route  
98 from a single stable equilibrium to chaotic behavior in the work of these authors consists of three successive Hopf  
99 bifurcations. The main difference between the two models is in the bifurcation threshold, which lies at smaller  
100  $Re$ -number in the baroclinic model, i.e., the latter is less stable than the barotropic one.

101 The purpose of the present paper is to examine the role of the baroclinic mode and of its interaction with the  
102 barotropic mode in the low-frequency variability of the double-gyre ocean circulation for time-constant wind stress.  
103 To do so, we select a model that provides a good balance between the wealth of fluid-dynamical processes it captures,  
104 on the hand, and its numerical simplicity, on the other. The latter feature will permit an exhaustive exploration of  
105 the model’s properties and an understanding of how qualitatively realistic behavior arises out of a minimal set of  
106 fluid-dynamical ingredients.

107 The oceanographic problem at hand involves several competing physical processes: wind-stress forcing at the sea  
108 surface, the strongly nonlinear dynamics in and near the western boundary currents, and the friction with the solid  
109 lateral and bottom boundaries. Flierl [21] showed that the calibration of a 2-layer QG model needs to be different to  
110 model correctly the role of wind stress, nonlinear advection in the ocean, and bottom friction, i.e., the depth of the  
111 interface between the layers and the density of each layer has to be set differently for each case. We chose therefore  
112 a QG model with *two modes* in the vertical, calibrated to study all three processes for the same set of parameters;  
113 this allowed us to investigate their competition adequately over a full parameter range.

114 This range contains parameter values that are close to those believed to apply to the real ocean. We emphasize  
115 the role of the deformation radius  $L_R$ , besides that of the wind-stress intensity  $\tau$ , in affecting solution behavior.

116 The model is presented in Section 2. A systematic dimensional analysis of the problem appears in Section 3.1. The  
117 dependence of numerical solutions on  $\tau$  and  $L_R$  is described in Section 3.2, while the energetics of the dynamical pro-  
118 cesses most active in different parts of the basin is reported in Section 3.3. Analytic steady-state solutions for a contin-  
119 uously stratified ocean are derived next, with symmetric solutions in Section 4.1 and asymmetric ones in Section 4.2;  
120 details of this derivation are given in Appendix A. The properties of the analytic solutions are compared in detail with

121 those of the steady-state solutions of our numerical QG model in Section 5.1, and with those of a shallow-water model  
 122 in Section 5.2. Our results are summarized in Section 6.1 and oceanographic inferences are drawn in Section 6.2.

## 123 2. The model

124 In this study, we use a QG rigid-lid model in which the vertical discretization is done by projection onto the  
 125 leading eigenmodes of the so-called vertical structure equation. Such a model, with up to four modes in the vertical,  
 126 has been used by Feliks [22] to study the evolution of isolated oceanic vortices and by Feliks and Ghil [23,24] to  
 127 study the meandering of and eddy detachment from baroclinic ocean jets.

128 The model equations are nondimensionalized by the following characteristic scales:

$$129 \quad X, Y \propto L, \quad Z \propto H, \quad T \propto \frac{L}{V}, \quad \psi \propto VL,$$

130 here  $L$  is the horizontal length scale and  $H$  the vertical scale, while  $V$  represents the particle speed at the base of  
 131 the permanent thermocline, i.e., at the fairly sharp interface between the ocean's more active upper layer and less  
 132 active lower layer. The appropriate scales and physical parameters for the North Atlantic are listed in Table 1, with  
 133  $L$  chosen as the characteristic length of the first baroclinic deformation radius at mid-latitudes (see Eq. (5) and the  
 134 paragraph that follows it).

135 The nondimensional potential vorticity (PV) equation with this scaling is

$$136 \quad \frac{\partial q}{\partial t} + \beta \frac{\partial \psi}{\partial x} + J(\psi, q) = r_H \nabla^4 \psi, \tag{1a}$$

137 where the relative PV is given by

$$138 \quad q \equiv \nabla^2 \psi + \frac{\partial}{\partial z} \left( \frac{1}{S} \frac{\partial \psi}{\partial z} \right), \tag{1b}$$

139 and the nondimensional parameters  $S$ ,  $\beta$  and  $r_H$  by

$$140 \quad S = \frac{N^2 H^2}{f^2 L^2}, \tag{1c}$$

$$141 \quad \beta = \beta_0 \frac{L^2}{V}, \tag{1d}$$

$$142 \quad r_H = \frac{E_H}{2\varepsilon} = \frac{A_H}{VL}, \tag{1e}$$

Table 1  
 Characteristic scales for the North Atlantic

$V$ (cm s <sup>-1</sup> )	5
$L$ (km)	50
$H$ (m)	4000
$T$ (days)	11.574
$\beta_0$ (cm <sup>-1</sup> s <sup>-1</sup> )	$1.8 \times 10^{-13}$
$\xi_{111}$	1.8
$\phi_1(0)$	4
$\phi_1(-H)$	-0.5
$A_H$ (cm <sup>2</sup> s <sup>-1</sup> )	$10^7$
$A_V$ (cm <sup>2</sup> s <sup>-1</sup> )	0.09
$f$ (s <sup>-1</sup> )	$8.37 \times 10^{-5}$

143  $f$  is the value of the Coriolis parameter at a central latitude ( $35^\circ\text{N}$ ),  $N = N(z)$  the mean Brunt–Väisälä frequency,  
 144  $\beta_0$  the meridional gradient of  $f$  at the central latitude,  $A_H$  the dimensional horizontal diffusion coefficient,  $\varepsilon = V/fL$   
 145 the Rossby number, and  $E_H = 2A_H/fL^2$  the horizontal Ekman number.

146 To compare the choice of nondimensional parameters in our model with other models that deal with the single- or  
 147 double-gyre circulation, we introduce the nondimensional widths  $\delta_M$  and  $\delta_I$  of the frictional and inertial boundary  
 148 layer, respectively. With the parameter values given in Table 1,  $\delta_M = [A_H/\beta L_*]^{1/3} = 1.48 \times 10^{-2}$ , where  $L_* =$   
 149  $2570$  km is the meridional extent of the integration domain, while  $\delta_I = 2\pi\tau_0/\rho_0\beta^2 H_* L_*^3$ , where  $H_* = 400$  m is  
 150 the typical depth of the upper layer in the models cited below. In our experiments  $4.8 \times 10^{-3} < \delta_I < 7.7 \times 10^{-3}$   
 151 or  $0.32 < \delta_I/\delta_M < 0.52$ . This choice of nondimensional parameters lies in the parameter region explored by Cessi  
 152 and Ierley [12], Speich et al. [14], Dijkstra and Katsman [18] and Chang et al. [25]. With the horizontal diffusion  
 153  $A_H$  chosen here, the typical Gulf Stream eddies that have a diameter of 200–300 km [26] are well resolved.

154 The upper boundary condition is

$$155 \quad w(x, y, z = 0, t) = \frac{1}{S} \frac{d}{dt} \left( \frac{\partial \psi}{\partial z} \right)_{z=0} = \frac{\tau_0}{\rho_0 f V \varepsilon} \text{curl } \tau_x, \quad (2a)$$

156 where  $\tau = \tau_0/\rho_0 f V \varepsilon$  is the nondimensional amplitude of the wind stress and its meridional profile  $\tau_x = \tau_x(y)$  is  
 157 given by

$$158 \quad \tau_x = \cos \left( \frac{2\pi y L}{L_a} \right). \quad (2b)$$

159 Here  $\tau_0$  is the dimensional amplitude, while  $L_a \cong L_*$  the meridional length scale of the domain and corresponds  
 160 to the characteristic scale of atmospheric wind shear. The lower boundary condition is imposed at  $z^* = H$  or  
 161  $z = z^*/H = 1$ , with dimensional variables denoted by an asterisk. It is given by

$$162 \quad w(x, y, z = 1, t) = \frac{1}{S} \frac{d}{dt} \left( \frac{\partial \psi}{\partial z} \right)_{z=1} = -r_V \nabla^2 \psi(z = 1), \quad (3)$$

163 where  $r_V = (2A_V f/H^2)^{1/2} L/V$ , and  $A_V$  is the dimensional vertical diffusion coefficient. It is important to note that,  
 164 in our model, the wind stress acts only through the upper boundary condition (2a) and (2b) and not as a body force,  
 165 like in JJG and Speich et al. [14]. A vertical Ekman number  $E_V$  is defined analogous to  $E_H$ , with  $A_V$  replacing  $A_H$ .

166 The lateral boundary conditions are chosen to be of partial slip,

$$167 \quad \psi = 0, \quad \frac{\partial q}{\partial n} = 0, \quad (4)$$

168 where  $n$  is the normal to the boundary, pointing east, west, north or south (i.e., in the  $x, -x, y$  or  $-y$  direction). The  
 169 reasons for the choice of partial-slip boundary conditions have been discussed in Section 1; in shallow-water models  
 170 they take a different form (see Appendix A of JJG). This boundary condition implies that there is no vorticity flux  
 171 through the sidewalls. The vorticity loss near the sidewalls, in the recirculation zone and other interior regions, such  
 172 as the eastward jet, where the flow is intense, arises from the vorticity flux through the bottom (see Eq. (3)).

173 The vertical structure of our model is based on the orthonormal eigenfunctions  $\phi_k(z)$  of the eigenvalue problem

$$174 \quad \frac{\partial}{\partial z} \left( \frac{1}{S} \frac{\partial \phi_k}{\partial z} \right) = -\lambda_k^2 \phi_k \quad (5)$$

175 with the boundary condition  $\partial \phi_k / \partial z = 0$  at the sea surface  $z = 0$  and at the mean depth  $z = 1$ . Here  $S$  is the Burgers  
 176 number defined in Eq. (1c); notice that  $\lambda_k^2 \sim 1/S$ . We designate by  $k = 0$  the barotropic mode and by  $k = 1, 2, \dots$ ,  
 177 the successive baroclinic modes. The *external* Rossby radius of deformation,  $L/\lambda_0$ , is infinite, according to the  
 178 rigid-lid assumption; the *k*th *internal* Rossby radius of deformation is  $L/\lambda_k$ ,  $k = 1, 2, \dots$ , and we shall retain in

179 our main analysis only  $k = 0$  and  $1$ . This limited vertical resolution still allows us to capture the main barotropic  
 180 and baroclinic processes of interest, as well as the interactions between the two. It also permits the fairly complete  
 181 investigation of phase-parameter space that will help us to elucidate the connections between the numerical solutions  
 182 of Section 3 and the analytic solutions of Section 4.

183 We decompose the streamfunction  $\psi$  and the PV  $q$  into vertical normal modes:

$$184 \quad \psi(x, y, z, t) = \sum_k \psi_k(x, y, t) \phi_k(z), \quad (6a)$$

$$185 \quad q(x, y, z, t) = \sum_k q_k(x, y, t) \phi_k(z). \quad (6b)$$

186 The equations for the modal amplitudes are [21]:

$$187 \quad \frac{\partial q_k}{\partial t} + \beta \frac{\partial \psi_k}{\partial x} + \sum_{i,j} \xi_{ijk} J(\psi_i, q_j) = r_H \nabla^4 \psi_k + \phi_k(0) w(z=0) - \phi_k(1) w(z=1), \quad (7)$$

188 where we retain here only  $k = 0, 1$ , and

$$189 \quad q_k = \nabla^2 \psi_k - \lambda_k^2 \psi_k, \quad \xi_{ijk} = \int_0^1 \phi_i \phi_j \phi_k dz, \quad (8)$$

190  $\xi_{ijk}$  are the triple interaction coefficients and the only one that is not zero or one hereafter is  $\xi_{111}$  (see Table 1).

191 The numerical scheme is the same as in [22,24]. Key features include fourth-order accurate discretization by finite  
 192 elements in the horizontal (cf. [27]), a second-order Adams–Bashforth scheme in time, and use of a fourth-order  
 193 Shapiro [28] filter at every time step. A uniform grid of  $257 \times 129$  points in the horizontal was used throughout  
 194 most of the numerical study, with a spatial and temporal resolution of  $L\Delta x = L\Delta y = 10$  km, and  $T\Delta t = 2700$  s.

195 Marshall and Marshall [29] showed that a 10 km resolution suffices to obtain the correct eastward penetration  
 196 scale of mid-latitude jets like the Gulf Stream, while a coarser resolution of 25 km dramatically reduces the pene-  
 197 tration length. Dijkstra and Katsman [18] also examined the convergence in phase-parameter space of the pitchfork  
 198 bifurcation point for their 1.5-layer model, as a function of grid resolution; they found that sufficiently accurate  
 199 results are obtained when the mesh size is no larger than 15 km.

200 At our 10 km resolution, the effect of the additional dissipation introduced by the Shapiro filter is quite small.  
 201 As we shall see in the next section, the typical diameter of the recirculation vortices is about 200 km, i.e., about  
 202  $20L\Delta x$ , while the filter acts to remove  $2L\Delta x$  wave components. The smallness of the filter’s effect on solution  
 203 behavior was tested and the results are reported in Section 3.2.

### 204 3. Numerical results

#### 205 3.1. Dimensional analysis

206 The continuously stratified model (1a)–(4) has the dependent variables  $\psi$  and  $q$  and the independent variables  $x$ ,  
 207  $y$ ,  $z$  and  $t$ . All the variables in the problem, dependent and independent, have dimensions that can be expressed in  
 208 terms of length  $L$  and time  $T$ . The vertically discretized model involves projection onto the eigenfunctions of the  
 209 problem (5). There are  $n = 11$  governing parameters of the discretized problem (1a)–(5):  $L_a$ ,  $L/\lambda_1$ ,  $H$ ,  $V$ ,  $\tau_0$ ,  $\beta_0$ ,  
 210  $A_H$ ,  $A_V$ ,  $\xi_{111}$ ,  $\phi(0)$  and  $\phi(-H)$ .

211 A simple consequence of the principle of scale invariance (or generalized homogeneity) of physical laws is the  
 212 fundamental theorem of scale analysis, often called (Buckingham’s)  $\pi$ -theorem (e.g., [30]): given a problem that

213 depends on  $n$  governing parameters in dimensional form and whose variables have  $d$  independent dimensions, the  
 214 results can be presented as a function of a minimal set of  $n - d$  nondimensional parameters. Here  $d = 2$  and thus  
 215  $n - d = 9$ ; a reasonable choice of the corresponding minimal set is  $\tau$ ,  $\epsilon$ ,  $E_H$ ,  $E_V$ ,  $S$ ,  $\beta$ , the aspect ratios  $H/L$  and  
 216  $L_a/L$ , and the normalized Rossby radius  $1/\lambda_1$ .

217 In this paper, we only examine the role of the wind stress  $\tau$  and the deformation radius  $L_R = 1/\lambda_1$  in the dynamics.  
 218 The role of  $r_H \sim E_H$  (see Eq. (1e)) was studied by JYG and Speich et al. [14], that of  $\beta$  and of the horizontal aspect  
 219 ratio  $L_x/L_y$  by Speich et al., and that of  $Re \sim r_H^{-1}$  and of the aspect ratio  $\delta$  between the thickness of their two  
 220 layers by Dijkstra and Katsman [18]. Moro [16,17], JYG and Dijkstra and Katsman [18] studied the effect of the  
 221 degree of partial slip (or no-slip vs. free-slip) at the lateral boundaries, which increase  $n$  by 1 in the count above.  
 222 Asymmetries in the wind-stress profile and smaller values of  $E_H$  were studied by Berloff and McWilliams [31] and  
 223 Simonnet et al. [32,33].

224 A more exhaustive study of the other parameters' effect on the model solutions is left for subsequent work. As  
 225 we shall see, however, in Section 6.1, the same basic bifurcation structure emerges, whichever parameter is varied  
 226 while the others are being kept fixed.

### 227 3.2. Solution dependence on $\tau$ and $L_R$

228 The steady-state numerical solutions for different values of the wind stress  $\tau$  and nondimensional deformation  
 229 radius  $1/\lambda_1$  are shown in Fig. 1, with the barotropic and baroclinic streamfunction in the left and right panels,  
 230 respectively. The features of the corresponding left and right panels are aligned almost perfectly with each other,  
 231 and are stronger in the first baroclinic mode. This mode is strongest near the surface, where the wind-stress forcing  
 232 is applied (see Eq. (2a)).

233 The spatial features of these circulations fall into three major patterns: (1) The basin-scale double-gyre cir-  
 234 culation, with its cyclonic gyre in the northern (or subpolar) part and the anticyclonic one in its southern (or  
 235 subtropical) part. (2) A strong western boundary current exists in each gyre, flowing towards the symmetry axis  
 236 of the wind stress, where the two currents merge into an eastward jet. (3) An intense mesoscale recirculation  
 237 occurs on either side of this axis, adjacent to the western boundary, for strong enough forcing. Thus our ide-  
 238 alized model captures the main features of the mid-latitude oceans' wind-driven circulation [7, and references  
 239 therein].

240 In the barotropic mode (left panels) the dipole structure formed by the two recirculation cells dominates, while  
 241 in the baroclinic mode this structure is embedded in the large-scale gyres; in other words, the barotropic mode is  
 242 confined, by-and-large, close to the separation points of the two western boundary currents. The circulation becomes  
 243 more vigorous as either  $\tau$  or  $L_R$  increases (see Table 2). We define the two poles of the dipole as the points where  
 244  $\psi$  reaches its largest relative values, i.e., its maximum and minimum. The scale  $R_d$  of the dipole is then defined as  
 245 the east–west distance between the more intense one of the two poles and the point to the “east” (i.e., at larger  $x$ ),  
 246 where  $\psi$  is equal to 1/3 of that extreme value. For given  $\tau$ , the scale  $R_d$  increases roughly by 0.2L as  $L_R$  increases  
 247 by 0.4L (see Table 3).

248 For  $1/\lambda_1 = 7/5$  and  $\tau \leq 0.0525$  a single (anti)symmetric solution branch is stable. For  $0.0525 \leq \tau \leq 0.0627$   
 249 asymmetric multiple equilibria appear through pitchfork bifurcation, as already shown by JYG and Dijkstra and  
 250 Katsman, due to the problem's symmetry. In Fig. 2, the bifurcation diagram is plotted for  $\Delta\psi_k = |\max \psi_k + \min \psi_k|$   
 251 as a function of  $\tau$  for both  $k = 0$  and 1; the quantity  $\Delta\psi_k$  measures the deviation of a given solution from being  
 252 (anti)symmetric. The parabola

$$253 \quad \tau = A_k(\Delta\psi_k)^2 + \tau_c \quad (9)$$

254 was fitted to the pairs of numerical results for  $k = 0, 1$ .

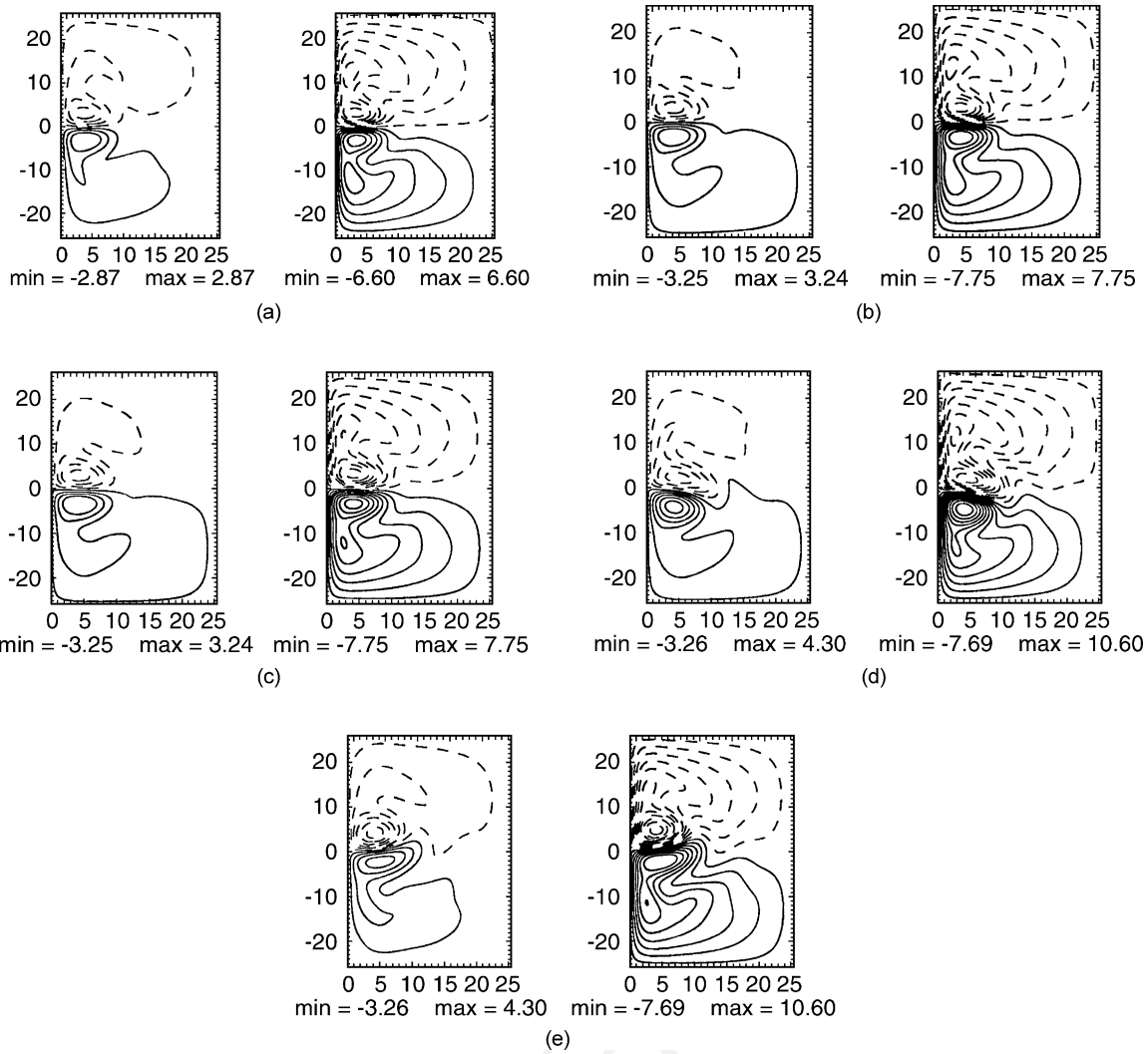


Fig. 1. The streamfunction of the model's steady-state solutions; the left panels show the barotropic mode, while the right panels show the baroclinic mode: (a)  $1/\lambda_1 = 3/5$ , (b)  $1/\lambda_1 = 1$  and (c)  $1/\lambda_1 = 7/5$ , all three for  $\tau = 0.051$ ; (d)  $1/\lambda_1 = 7/5$  and (e)  $1/\lambda_1 = 3$ , both for  $\tau = 0.0588$ . Contour intervals are 0.7 for the left and 1.0 for the right panels; minimum and maximum values appear as legends below each panel

255 The critical point  $\tau_c$  is the point where the parabola intersects the  $\tau$ -axis passing through  $\Delta\psi_k = 0$ . This point  
 256 is independent of  $k$ , i.e., the two parabolas—for the barotropic and baroclinic modes—intersect the  $\tau$ -axis in the  
 257 same point. From (9) we find that the ratio

$$258 \left( \frac{\Delta\psi_0}{\Delta\psi_1} \right)^2 = \frac{A_1}{A_0} = 0.12 \tag{10}$$

259 is a constant. For all  $\tau$ ,  $|\Delta\psi_k|$  for  $k = 1$  is larger by a factor of 2.9 than for  $k = 0$ . These results represent an  
 260 important confirmation of the crucial role played by the pitchfork bifurcation in the double-gyre problem, whether  
 261 baroclinic processes are present or not. For  $\tau > 0.0627$  a periodic solution arises by Hopf bifurcation from either

Table 2

Dependence of the circulation's intensity  $|\psi_k|_{\max}$  and symmetry  $\Delta\psi_k$  on inverse deformation radius  $\lambda_1$  and wind-stress intensity  $\tau$  for  $k = 0$  (left column) and  $k = 1$  (right column)

$1/\lambda_1$	$\tau$	$ \psi_k _{\max}$		$\Delta\psi_k$	
3/5	0.0398	1.77	4.52	0	0
3/5	0.051	2.87	6.60	0	0
1	0.0398	1.95	4.88	0	0
1	0.051	3.25	7.75	0.01	0
6/5	0.0548	3.87	9.45	0.61	1.74
7/5	0.051	3.29	8.02	0	0
7/5	0.053	3.66	8.99	0.39	1.14
7/5	0.0548	3.90	9.64	0.66	1.93
7/5	0.0588	4.30	10.6	1.04	2.91
9/5	0.0588	4.32	10.8	1.08	3.08
3	0.051	3.49	8.73	0.27	0.79
3	0.0588	4.33	11.0	1.13	3.26

Table 3

Comparison of the key solution properties between the analytical solution and the numerical QG solution for a few values of the main parameters  $\lambda_1$  and  $\tau$ ;  $\psi_{\max}$  is the maximum within the numerical dipole of the flow pattern at the surface, given by  $|\psi_0(x, y) + \phi_1(0)\psi_1(x, y)|$  (see text for details)

Control parameters		Numerical solution		Analytical solution	
$1/\lambda_1$	$\tau$	$\alpha$	$\psi_{\max}$	$R_d$	$R_d^{(a)}$
3/5	0.0398	-1.59	19.85	3.8	4.0
3/5	0.051	-1.08	29.27	4.6	4.5
1	0.0398	-1.42	21.47	4.0	4.2
1	0.051	-1.01	34.25	4.8	5.1
7/5	0.051	-1.0	35.37	5.0	5.3

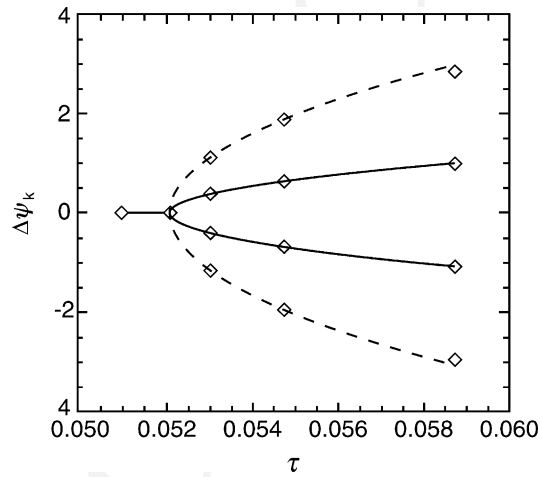


Fig. 2. Computed pitchfork bifurcation diagram as a function of the wind-stress intensity  $\tau$ , for  $1/\lambda_1 = 7/5$ . Values on the ordinate represent the solution's degree of asymmetry (i.e., its deviation from exact antisymmetry), as measured by  $\Delta\psi_k$ ; barotropic mode ( $k = 0$ ), solid line; baroclinic mode ( $k = 1$ ), dashed line. The fitted parabola is given by Eq. (9), with  $A_0 = 6.17 \times 10^{-3}$ ,  $A_1 = 7.22 \times 10^{-4}$ , and  $\tau_c = 5.2 \times 10^{-2}$ .

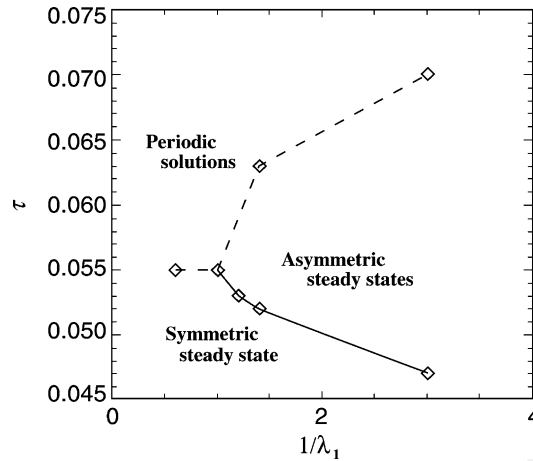


Fig. 3. The catastrophe diagram with respect to  $\tau$  (on the ordinate) and the nondimensional Rossby radius of deformation  $1/\lambda_1$  (on the abscissa).

262 steady-state branch. This solution is characterized by a liberation [34]—i.e., a rocking back and forth—of the dipole  
 263 around the intersection of the straight line that connects its two poles (that is, the two opposite extrema of the  
 264 streamfunction  $\psi$ ) with the axis of symmetry of the wind stress; we shall refer to the former straight line as the  
 265 centerline of the dipole. The liberation of the periodic solution that arises from the upper equilibrium branch is a  
 266 mirror image of that observed in the lower-branch periodic solution. For  $\tau > 0.0675$  the solutions become chaotic.

267 For  $1/\lambda_1 \leq 1$ , a single steady-state branch of symmetric solutions is obtained as long as  $\tau \leq 0.051$ . As  $\tau$   
 268 increases past this point, periodic solutions appear due to Hopf bifurcation. No stable asymmetric equilibria are  
 269 found, indicating that the pitchfork bifurcation stage is skipped for small deformation radii. For all  $L_R$  values larger  
 270 than (nondimensional) unity that we have investigated, the transition to chaos is as described above for the particular  
 271 value  $\lambda_1 = 5/7$ . Increase in  $1/\lambda_1$  or  $\tau$  result in increased  $\Delta\psi_k$  (Table 2).

272 In Fig. 3 the catastrophe diagram of the solutions is shown as a function of  $\tau$  and  $1/\lambda_1$ . At low values of the two  
 273 parameters, the (anti)symmetric steady-state solution is unique and stable. Multiple asymmetric stable equilibria  
 274 prevail for values of  $\tau$  between the full and dashed lines. Periodic solutions were obtained for values of  $\tau$  above the  
 275 dashed line.

276 These results are consistent with those of Dijkstra and Katsman, who examined the bifurcation of their 2-layer  
 277 QG model for  $L_R = 30$  km (i.e.,  $1/\lambda_1 = 3/5$ ) as a function of  $Re \sim r_H^{-1}$ . They found a situation that is equivalent to  
 278 our results for  $1/\lambda_1 \leq 1$ , with Hopf bifurcation to limit cycles from the unique stable branch preceding the pitchfork  
 279 bifurcation to multiple stable equilibria.

280 We examine in greater detail the periodic solution for  $1/\lambda_1 = 3/5$  and  $0.059 \leq \tau \leq 0.067$ . For  $\tau = 0.059$  the  
 281 dominant period is 10.4 years (see Fig. 4). There is a phase shift of one quarter period between the two modes,  
 282 with the baroclinic mode (dashed line) leading the barotropic one (solid line). As  $\tau$  increases to 0.067, the period  
 283 decreases to 1.7 years, while the  $\pi/2$  shift between modes persists, indicating the baroclinic nature of the instability;  
 284 a similar phase shift between their two layers was found by Dijkstra and Katsman [18].

285 We see that the relative role of baroclinic and barotropic processes in breaking the spatial and temporal symmetry of  
 286 the unique steady-state solution that obtains at low forcing depends on the Rossby radius of deformation: the smaller  
 287 this radius, the more decisive the role of the baroclinic processes. The dimensional value of  $L_R = L/\lambda_1 = 50$  km,  
 288 at which the two bifurcations in Fig. 3 coincide, corresponds roughly to that prevailing at mid-latitudes in the North  
 289 Atlantic [22–24].

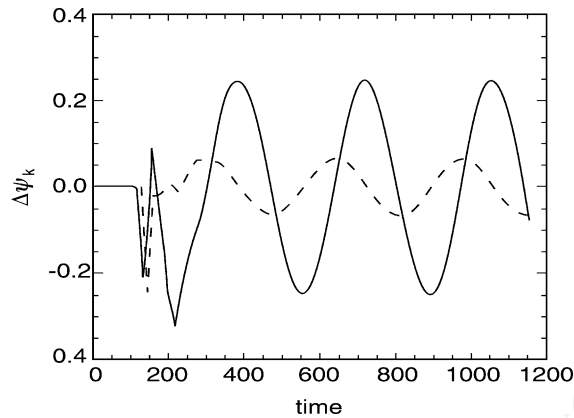


Fig. 4. Periodic solution for  $\tau = 0.059$  and  $1/\lambda_1 = 3/5$ : the evolution in time of the streamfunction field's asymmetry  $\Delta\psi_k$ ;  $k = 0$  (solid line),  $k = 1$  (dashed line). The nondimensional time unit corresponds to 11.574 days.

290 The period of 1.7 years found here is close to that found in [18], i.e. 1.5 years; Dijkstra and Katsman found no  
 291 longer periods, since they kept  $\tau$  fixed. In our periodic regime, the amplitude of the anomaly streamfunction—i.e.,  
 292 of the difference between the instantaneous field and the mean field—in the barotropic mode is about 10% of the  
 293 mean (not shown) and it is about 1% in the baroclinic mode. The periodic solutions' barotropic mode amplitude is  
 294 itself substantial only in the highly nonlinear recirculation zone. In the next section we show that the double-gyre  
 295 circulation's key instability does arise, in fact, in the recirculation region.

296 As  $\tau$  increases, the amplitude of the anomalies and the liberation angle of the dipole's centerline also increase.  
 297 When  $\tau$  crosses a critical value that also depends on  $1/\lambda_1$  (not shown), the solution becomes chaotic, i.e. the  
 298 evolution of the dipole is no longer periodic. The flow-field evolution is shown for  $1/\lambda_1 = 3/5$  and  $\tau = 0.078$ —just  
 299 after the transition to chaos—in Fig. 5a for the barotropic mode and in (b) for the baroclinic mode. At this value  
 300 of the Rossby deformation radius, the actual transition occurs at  $\tau = 0.069$ . Between this value and the one shown  
 301 in Fig. 5, the solutions exhibit essentially the same sequence of flow patterns, but the amplitude and period of this  
 302 sequence changes from one cycle to the next, at the same  $\tau$ -value. Thus, although the solution is aperiodic, Fig. 5  
 303 corresponds roughly to one half of the life cycle of this variable sequence.

304 The dipole's centerline starts by being perpendicular to the symmetry axis  $y = 0$  and dips NE–SW as the  
 305 stronger recirculating vortex, south of the axis, pulls the weaker one clockwise. The downstream meander is  
 306 weakened in the process and the cyclonic vortex, elongated along the eastern portion of the anticyclonic one,  
 307 breaks into two smaller vortices that occupy positions north and south of the major, negative-vorticity feature.  
 308 Next, the eastern tip of the dipole's cyclonic vortex begins to wrap around the anticyclonic pole. Further east-  
 309 ward, outside the dipole region, a new meander begins to develop in the eastward-flowing jet. The dimensional  
 310 wavelength of the meander is about 400 km; this equals the length of the most unstable wave found by Feliks  
 311 and Ghil [24]. Finally, an eddy detaches from the cyclonic vortex, which has wrapped by now around half the  
 312 periphery of the anticyclonic one (Fig. 5a); in the baroclinic mode, this eddy detachment occurs slightly later and is  
 313 not shown.

314 The amplitude and structure of the barotropic component of the basin-scale gyres changes but little with time.  
 315 Since all the streamlines in these two gyres are condensed and pass through the small-area dipole, weak changes in  
 316 the former are associated with strong changes in the latter.

317 We carried out a simple test to ascertain the robustness of our bifurcation results to the numerical dissipation  
 318 introduced by the Shapiro filter (see Section 2), and turned the filter off altogether in a number of cases. Haidvogel

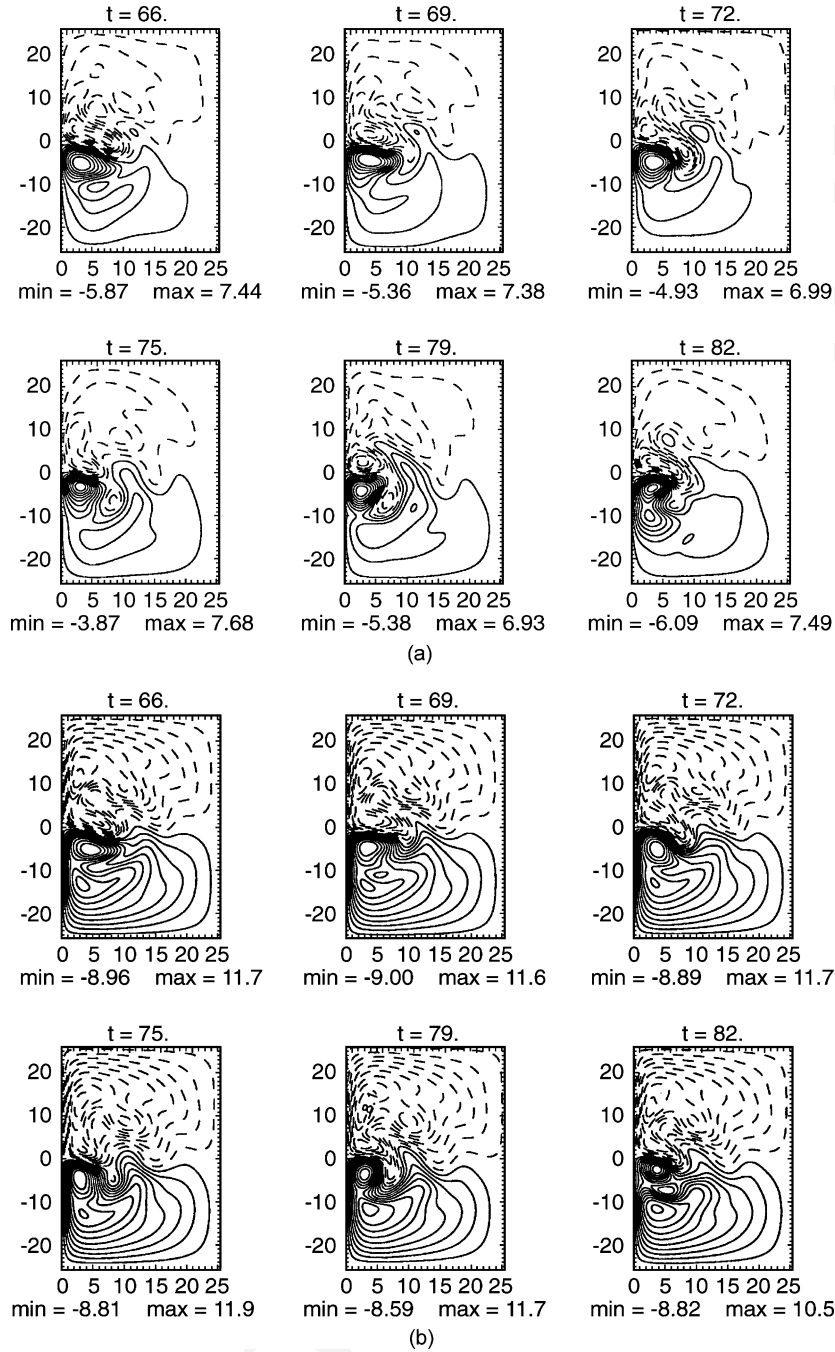


Fig. 5. The evolution of the streamfunction field in time for  $\tau = 0.078$  and  $1/\lambda_1 = 3/5$ : (a) barotropic mode; (b) baroclinic mode; contour intervals as in Fig. 1.

319 et al. [27] showed, in fact, that the filter's damping of wavelengths beyond  $5L\Delta x$  is quite small; since our smallest  
 320 subgyres are about  $20L\Delta x$  in size, we expect the filter's effect on the flow patterns to be fairly minimal.

321 The numerical experiments without the filter were carried out at deformation radii  $1/\lambda_1 = 3/5, 1$  and  $7/5$ . The  
 322 largest differences between the steady-state solutions obtained with and without filter occurred in the dipole region;  
 323 they never exceeded 8% in the streamfunction  $\psi$  and 5% in the relative PV. As  $\tau$  is increased for fixed  $1/\lambda_1$ , the  
 324 Hopf bifurcation points move very little: the critical value  $\tau_c$  is 0.049 for  $1/\lambda_1 = 3/5$  and 0.051 for  $1/\lambda_1 = 1$   
 325 without the filter vs. 0.055 for both deformation radii with the filter. Recall that for these two  $\lambda_1$  values, the Hopf  
 326 bifurcation point precedes the pitchfork bifurcation (see again Fig. 3). For  $1/\lambda_1 = 7/5$ , the pitchfork bifurcation  
 327 occurs at  $\tau_c = 0.052$  and the Hopf bifurcation at 0.063, whether the filter is turned on or off.

328 These small effects support the analysis of Feliks and Ghil [24], who showed (see Eq. (26) there) that the  
 329 fourth-order Shapiro (1970) filter is equivalent to adding another fourth-order diffusion term to the right-hand side  
 330 (RHS) of Eq. (27) for the modal amplitudes. This is the same as adding a coefficient  $r'_H$  to the coefficient  $r_H$  already  
 331 present in the equation, with  $r'_H = (1/16)(\Delta x)^4/\Delta t$ . For the resolution used here, of  $\Delta x = \Delta y = 10 \text{ km}/L$  and  
 332  $\Delta t = 2700 \text{ s}/T$ ,  $r'_H = 7.4 \times 10^{-6}$  in nondimensional units or  $-A = 2.3 \times 10^{19} \text{ cm}^4 \text{ s}^{-1}$ , in the notation of Feliks  
 333 and Ghil (the minus sign here corrects the typographic error in Eq. (26) of the earlier paper). The slight lowering of  
 334 the bifurcation point as the effective dissipation is reduced—due to the filter's removal—is entirely consistent with  
 335 the rest of our numerical results.

### 336 3.3. Physical properties of the solutions

337 The three major spatial patterns mentioned in the previous section—basin-scale double-gyres, western boundary  
 338 currents, and mesoscale dipole—are present in all the (anti)symmetric and asymmetric equilibria, as well as in the  
 339 periodic and chaotic solutions. In this section, we study in detail the balance between the different terms of the  
 340 modal PV equation (7) in each one of the three subdomains. This balance is presented here for the stable steady-state  
 341 (anti)symmetric solution that is obtained for  $\lambda_1 = 1$  and  $\tau = 0.051$ .

342 We label the three subdomains W for the *western boundary currents*, D for the *dipole*, and G for the remainder of  
 343 the domain, where the basin-scale portion of the *gyres* completes the circulation. The dominant terms in the largest  
 344 subdomain, the G region, are the  $\beta$ -term,  $\beta(\partial\psi_k/\partial x)$ , and the wind-stress curl term  $\phi_k(0)w(z=0)$ ; all other terms  
 345 in Eq. (7) are smaller by an order of magnitude. Thus the curl of the wind stress is balanced by the  $\beta$ -term, and the  
 346 G region is dominated by the Sverdrup relation, in both the barotropic and baroclinic modes (see Chapters 2 and 3,  
 347 respectively, of [7]).

348 In the W region the dominant terms are the  $\beta$ -term  $\beta(\partial\psi_k/\partial x)$ , lateral diffusion  $r_H\nabla^4\psi_k$  and nonlinear advection  
 349  $\xi_{k11}J(\psi_1, q_1)$ , for both  $k = 0$  and  $1$ . Off the coast and up to a distance of  $3/5$  from it, the  $\beta$ -term is balanced by  
 350 the horizontal friction in a Munk [2] layer;  $x = 3/5$  is the nondimensional width of the frictional boundary layer  
 351 obtained for  $r_H$  as given by the dimensional  $A_H$  in Table 1. Further eastward the role of the nonlinear advection term  
 352 increases and that of the friction decreases (not shown). So, at unit distance off the coast, the  $\beta$ -term is balanced  
 353 by the nonlinear advection term in an inertial boundary layer [6]. Where either boundary current separates from the  
 354 coast, the nonlinear advection term has a role equal to the horizontal friction at a distance smaller than  $3/5$  off the  
 355 coast as well.

356 In this paper we are mainly interested in the recirculating dipole region D. In this region the dominant terms in  
 357 the barotropic mode— $J(\psi_1, q_1)$ ,  $\beta(\partial\psi_0/\partial x)$ , and  $r_H\nabla^4\psi_0$ —are shown in Fig. 6a–c, respectively. The  $\beta$ -term has  
 358 the same sign as the vorticity for either pole of the dipole, hence it tends to intensify it. This term is larger in the  
 359 western than in the eastern part of the dipole (compare Fig. 6b with Fig. 1b) and thus it tends to propagate the dipole  
 360 westward. The nonlinear advection term  $-J(\psi_1, q_1)$  has the opposite sign and a similar west-to-east amplitude  
 361 gradient, so that it tends to weaken the dipole and propagate it eastward. This type of balance also holds for modon

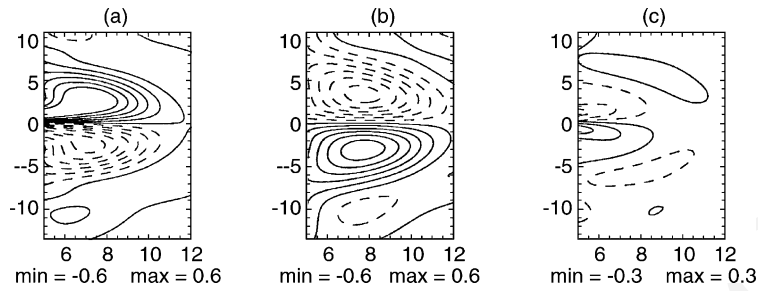


Fig. 6. The tendency terms in the PV equation (7) for the (anti)symmetric steady state obtained for  $\tau = 0.051$  and  $\lambda_1 = 1$ ; shown for the dipole region D and in the barotropic mode: (a)  $J(\psi_1, q_1)$ ; (b)  $\beta\partial\psi_0/\partial x$ ; (c)  $r_H\nabla^4\psi_0$ ; contour intervals are equal to 0.1.

362 and dipole solutions in the open ocean (e.g., [22,23,25]). In the dipole’s western part, where the eastward jet enters  
 363 it (see Fig. 1), nonlinear advection is balanced by horizontal friction and the  $\beta$ -effect.

364 The dominant terms in the baroclinic mode for region D— $J(\psi_0, q_1) + J(\psi_1, q_0)$ ,  $\xi_{111}J(\psi_1, q_1)$ ,  $\beta(\partial\psi_1/\partial x)$ ,  
 365 and  $r_H\nabla^4\psi_1$ —are shown in Fig. 7a–d, respectively. The last three of these (Fig. 7b–d) have the same role here as the  
 366 corresponding terms of Fig. 6a–c for the barotropic mode. In the baroclinic mode, the “mixed” barotropic–baroclinic  
 367 advection term of Fig. 7a plays the same role as the “pure” baroclinic–baroclinic term of Fig. 7b, since they have  
 368 the same sign, although the former is considerably weaker.

369 As the above analysis shows, nonlinear advection terms are important in the dipole region D and slightly less so in  
 370 the western boundary region W. The curl of the wind stress plays a key role within the basin-scale region of the double-  
 371 gyre circulation G, but can be neglected inside the D and W regions. Horizontal friction is important in the western

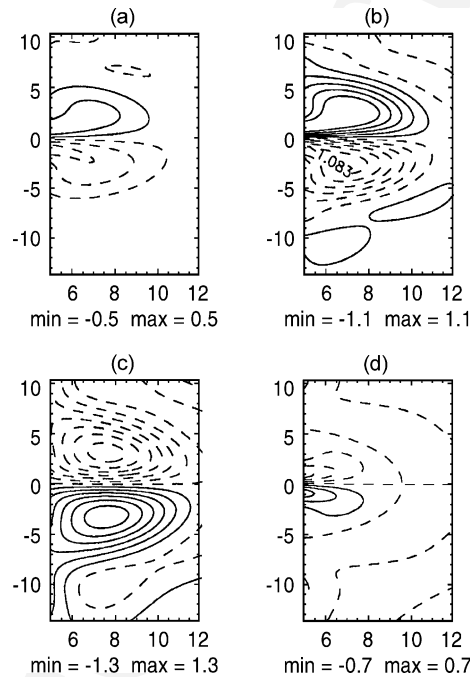


Fig. 7. Same as Fig. 6 for the baroclinic mode: (a)  $J(\psi_0, q_1) + J(\psi_1, q_0)$ ; (b)  $\xi_{111}J(\psi_1, q_1)$ ; (c)  $\beta\partial\psi_1/\partial x$ ; (d)  $r_H\nabla^4\psi_1$ ; contour intervals are equal to 0.2.

372 boundary currents, and in the dipole's western part. The  $\beta$ -term is crucial throughout all three subdomains, while  
 373 bottom friction—which enters through the boundary conditions, via Eqs. (3) and (7)—has only a secondary effect.

374 Because of the nonlinear terms' importance in the dipole region D, this region is often referred to as the “inertial  
 375 recirculation zone” in the oceanographic literature [7,36–38]. The importance of the inertial nonlinearity in this  
 376 region emphasizes its key role in the successive bifurcations undergone by the entire basin's double-gyre circulation,  
 377 and the circulation's ultimate transition to chaos. It is thus not surprising to see most of the “action”, i.e. the changes  
 378 in flow patterns, occur in the dipole region. The unstable oscillatory mode that gives rise to the Hopf bifurcation in the  
 379 model has its largest amplitude in the dipole region and decays away from it in concentric ellipses (not shown here, but  
 380 see [14] for an illustration of this behavior in a shallow-water model and [18] for the same behavior in a QG model).

#### 381 4. Dipole solutions in a stratified ocean

382 Given the obvious importance of the dipole region D in the more or less regular behavior of the entire basin's  
 383 double-gyre circulation, we examine here the dipole-shaped analytical solutions to the steady-state PV equation in  
 384 a continuously stratified ocean. We saw, indeed, in Section 3.3 that the main dynamic balance in the dipole region is  
 385 between the advective terms and the  $\beta$ -term and so we seek an appropriate three-dimensional (3D) generalization  
 386 of ‘free modes,’ such as Stern's [39] modon or Larichev and Reznik's [40] solitary Rossby waves.

387 The nonlinear free modes obtained below can be resonantly excited by the confluence and eastward extension  
 388 of the western boundary currents. Greatbatch [37,38] discusses the potential importance of such free modes for the  
 389 wind-driven, laterally dissipated ocean circulation, while Branstator and Opsteegh [41] and Marshall and So [42]  
 390 discuss the analogous importance of exciting such free modes in the low-frequency variability of atmospheric flows.  
 391 The key properties of the analytic solutions derived in Sections 4.1 and 4.2 will be compared in Section 5.1 with  
 392 those of our QG model's dipole region (see Section 3) and in Section 5.2 with those of the same region in JGs  
 393 shallow-water model.

##### 394 4.1. Antisymmetric analytical solution

395 The analytical free modes obtained in this section and the next one are solutions of the steady-state inviscid PV  
 396 equation in a continuously stratified ocean:

$$397 \quad J \left[ \psi, \nabla^2 \psi + \frac{\partial}{\partial z} \left( \frac{1}{S} \frac{\partial \psi}{\partial z} \right) + \beta y \right] = 0. \quad (11)$$

398 Their origin is co-located with the center of the numerical dipole, i.e. the point where the straight line segment  
 399 connecting the poles of the numerical dipole intersects the  $x$ -axis. Eq. (11) is a more restricted form of Eqs. (1a)  
 400 and (1b) in two ways: it governs steady-state solutions of (1a)–(1e) and it represents its limit for weak forcing and  
 401 dissipation [43–45]. Conditions under which solutions of (11) may be good approximations of those of (1a)–(1e)  
 402 in our case are discussed at the end of Sections 5.1 and 6.1.

403 Because the Jacobian in (11) vanishes, there is an arbitrary functional dependence between the absolute PV,  
 404 defined as  $Q \equiv q + \beta y$ , and the streamfunction  $\psi$ . Following Bretherton and Haidvogel [46] and McWilliams and  
 405 Flierl [35], among others, assume that this function is piecewise linear, i.e.,

$$406 \quad \nabla^2 \psi + \frac{\partial}{\partial z} \left( \frac{1}{S} \frac{\partial \psi}{\partial z} \right) + \beta y = \alpha \psi + q_0, \quad (12)$$

407 here  $\alpha$  and  $q_0$  can be a constant or a function of  $z$  (see [37]) and have different values in different regions.

408 The barotropic case of (12) was examined by Fofonoff [3], who found two types of solutions. When  $\alpha > 0$  the  
 409 solution has two large gyres: cyclonic in the northern part of the basin ( $y > 0$ ) and anticyclonic in its southern  
 410 part ( $y < 0$ ), with an inertial boundary layer along the solid boundaries. This solution will be called as *F-type* (for  
 411 Fofonoff). When  $\alpha < 0$  no inertial boundary layer exists and the solution has small-scale eddy structure ([3]; see  
 412 also the discussion in [38]).

413 Marshall and Nurser [47] examined both the barotropic and baroclinic case of Eq. (12) in a multi-layer model  
 414 with  $q_0 = \beta(L_a/2)f(z)$  for  $y > 0$  and  $q_0 = -\beta(L_a/2)f(z)$  for  $y < 0$ , where

$$415 \quad f(z) = \begin{cases} 1, & z < h_1, \\ 0, & z > h_1, \end{cases} \quad (13)$$

416 and  $h_1$  is the depth of their upper layer. They obtained two large gyres, with a strong jet flowing eastward between  
 417 the gyres and a weak flow along the southern and northern boundaries. This solution resembles the double-gyre  
 418 structure of our numerical solutions and such a free mode can be resonantly excited by the wind stress. In our  
 419 results, however, the dynamic balance of the G region is between the  $\beta$ -term and the curl of the wind stress, while  
 420 the nonlinear advection terms are quite small (see Section 3.3).

421 Marshall and Marshall [29] examined the seaward-flowing inertial jet along the northern rim of a subtropical gyre  
 422 in a barotropic QG model. They showed that, when the jet profile at the inflow has a linear functional dependence  
 423 between  $Q$  and  $\psi$ , with  $\alpha > 0$ , the jet penetrates all the way to the eastern boundary, i.e. it resembles the equatorward  
 424 part of an F-type solution. When  $\alpha < 0$  they obtained the lower part,  $-\pi < \theta < 0$ , of Stern's [39] modon as a  
 425 solution:

$$426 \quad \psi_0 = \begin{cases} \frac{\beta r_0}{k^2[(J_1(kr)/J_1(kr_0)) - (r/r_0)] \sin \theta}, & r < r_0, \\ 0, & r > r_0, \end{cases} \quad (14)$$

427 where  $kr_0 = 5.136$ ,  $k^2 = -\alpha$  for  $r < r_0$  and  $\alpha \rightarrow \infty$  for  $r \geq r_0$ , i.e. the jet recirculates rather than extending  
 428 further eastward. The zonal scale of the jet's penetration into the basin is (see also [38]):

$$429 \quad r_0 = 5.136|\alpha|^{-1/2}. \quad (15)$$

430 Marshall and Marshall [29] also applied their analysis to a 2-layer baroclinic ocean model. For this model, their  
 431 analytical solution is the sum of a pseudo-barotropic mode A and a pseudo-baroclinic mode B. Mode A is still  
 432 the lower part of Stern's modon, while mode B is a zonal flow given by a streamfunction that is linear in  $y$ . Their  
 433 derivation seems to suffer, however, from a technical difficulty: for each layer, the vorticity is discontinuous on  
 434  $r = r_0$  due to the use of the Stern modon solution in their mode A. Thus  $r = r_0$  has to be a streamline in each layer,  
 435 but, in their solution for each layer, the streamfunction is not constant along  $r = r_0$  due to their mode B.

436 For  $\alpha < 0$ , no solution for a multi-level or truncated-mode model seems to be free of this conceptual problem  
 437 when following the approach of these authors. Greatbatch [37,38] explored, in fact, the continuously stratified case  
 438 by the traditional separation of variables [6] into vertical and horizontal modes. He found that only solutions that  
 439 have a finite number of modes in the vertical were compatible with  $\alpha < 0$ ; they were thus the only ones that could  
 440 have closed, recirculating streamlines. We looked therefore for an analytical solution to the continuous 3D problem  
 441 governed by Eq. (12) and used a different type of vertical stratification than that of the previous authors, as well as  
 442 spherical rather than Cartesian or cylindrical coordinates.

443 Taking the stratification parameter  $S$ , as defined in Eq. (1c), to be of the form

$$444 \quad N^2 = \frac{N_B^2}{z^{2\delta}}, \quad \delta \geq 0, \quad (16)$$

445 allows Eq. (12) to be solved analytically in closed-form, rather than by separation of variables. The profile of  $N^2$   
 446 in (16) has qualitative similarity with that found in the real ocean when  $N_B^2$  is the value of  $N^2$  near the bottom of  
 447 the sea, at 4 km, say: this value is about four orders of magnitude smaller than that at the bottom of the mixed layer,  
 448 40 m below the sea surface, say; see [48,49] and further references there for the goodness-of-fit between analytic  
 449 profiles like (16) and the actual stability profile for the North Atlantic.

450 We introduce a new vertical coordinate

$$451 \quad z_* = \frac{\Gamma}{\eta} z^\eta, \quad (17)$$

452 where  $\Gamma = N_B H / fL$  and

$$453 \quad \eta = 1 - \delta \geq 0, \quad (18)$$

454 so that both  $\delta$  and  $\eta$  lie between 0 and 1. In this coordinate,

$$455 \quad \frac{\partial}{\partial z} \left( \frac{1}{S} \frac{\partial \psi}{\partial z} \right) = \frac{\delta}{\eta z_*} \frac{\partial \psi}{\partial z_*} + \frac{\partial^2 \psi}{\partial z_*^2}, \quad (19)$$

456 and Eq. (12) takes the form:

$$457 \quad \nabla^2 \psi + \frac{\partial^2 \psi}{\partial z_*^2} + \frac{\delta}{\eta z_*} \frac{\partial \psi}{\partial z_*} + \beta y = \alpha \psi. \quad (20)$$

458 The boundary conditions for Eq. (11) in a horizontally infinite domain are the homogeneous counterparts of  
 459 Eqs. (2a)–(3), i.e.,

$$460 \quad w(x, y, z) = \frac{1}{S} \frac{d}{dt} \left( \frac{\partial \psi}{\partial z} \right)$$

461 at  $z = 0, 1$ , i.e., at  $z_* = 0, \Gamma/\eta$ .

462 A solution to Eq. (20) in spherical coordinates

$$463 \quad x = r \sin \theta \cos \varphi, \quad y = r \sin \theta \sin \varphi, \quad z_* = r \cos \theta \quad (21)$$

464 with these boundary conditions, is given by

$$465 \quad \psi = \left[ A \frac{J_\nu(kr)}{(kr)^{\nu-1}} - \frac{\beta}{k^2} r \right] \sin \theta \sin \varphi, \quad r < r_0, \quad (22a)$$

$$466 \quad \psi = - \left[ B \frac{K_\nu(pr)}{(pr)^{\nu-1}} - \frac{\beta}{p^2} r \right] \sin \theta \sin \varphi, \quad r > r_0. \quad (22b)$$

467 Here  $J_\nu$  and  $K_\nu$  are the Bessel and modified Bessel functions of the first kind and of order  $\nu = (3 + \delta/\eta)/2$ , as  
 468 explained in Appendix A. Given the relation (18) between  $\delta$  and  $\eta$ ,  $\nu = \nu(\delta)$  is a monotonically increasing function  
 469 of  $\delta$  for  $\delta \geq 0$  and

$$470 \quad \nu = \frac{3 - 2\delta}{2(1 - \delta)} \geq 0. \quad (23)$$

471 The parameters  $-k^2$  and  $p^2$  are the coefficients of proportionality between  $Q$  and  $\psi$  inside and outside the dipole,  
 472 respectively. There is no connection between the parameter  $k$  here and the index of the vertical modes used as a  
 473 subscript in Eq. (5) and throughout Sections 2 and 3 thereafter.

474 The constants  $A$  and  $B$  are given by Eq. (A.5). The particular case of a 3D modon for constant stratification, i.e.,  
 475  $\delta = 0$  and thus  $\nu = 3/2$ , was first obtained by Berestov [50].

476 The conditions for the absolute PV  $Q$  and the velocity to be continuous on  $r = r_0$ —the outermost closed  
 477 streamline at the fluid’s surface—are also derived in Appendix A. They yield a range

478 
$$a = \min(kr_0) \leq kr_0 \leq \max(kr_0) = b \tag{24}$$

479 within which the key solution parameter  $kr_0$  must lie.

480 The interval (24) is a function of the parameter  $\nu$ , and is found as follows. When the bracketed term in Eq. (A.6a)  
 481 is negative, the spatial pattern of the analytic solution resembles the dipole of the numerical solution, i.e. a cyclonic  
 482 eddy lies north of the  $x$ -axis and an anticyclonic one lies to the south. This is so for  $J_\nu(kr_0) \leq 0$ ;  $J_\nu(a) = 0$  thus yields  
 483  $a$  in (24) as the first node of  $J_\nu$ . The RHS of (A.8) is always nonnegative. Thus one must have  $J_{\nu+1}(kr_0) \geq 0$ , for  
 484 the left-hand side of (A.8) to be nonnegative. Equality with the RHS of (A.8) can be fulfilled provided  $J_{\nu+1}(b) = 0$ ,  
 485 where  $b$  is the first node of  $J_{\nu+1}$  and thus  $b > a$ . Since  $K_\nu(pr)$  decays exponentially to zero in the outer domain  
 486  $r > r_0$ ,  $\psi$  tends exponentially to  $(\beta/p^2)y$  there, i.e. to a barotropic mode, and  $1/p$  is the  $e$ -folding length of this decay.

487 Consider next some properties of the analytical solution (22a) and (22b) or, more precisely, (A.6a) and (A.6b)  
 488 subject to the continuity condition (A.8), for values of  $\nu$  given by (23). These properties will help us later to compare  
 489 the analytical and numerical solutions. For a constant stratification,  $\delta = 0$ , we obtain  $\nu = 3/2$  and thus  $a = 4.49$   
 490 and  $b = 5.76$  in Eq. (24), while for the stratification used in the numerical solutions of Section 3,  $\delta = \eta = 1/2$  and  
 491 thus  $\nu = 2$ , which yields  $a = 5.13$  and  $b = 6.38$ .

492 When  $J_{\nu+1}(b)=0$ ,  $pr_0 \rightarrow \infty$  according to the RHS of (A.8). In this case,  $\psi \equiv 0$  for  $r > r_0$  and the special  
 493 solution so obtained can be considered as an extension of Stern’s [39] modon into three dimensions. A generalization  
 494 of the classical modon solution from a QG to a shallow-water model in two dimensions has been outlined by Sakuma  
 495 and Ghil [51].

496 In Fig. 8,  $pr_0$  is shown as a function of  $kr_0$  for two cases of Eq. (23),  $\nu = 3/2$  and 2. The first one corresponds  
 497 to the lower bound  $\nu = 3/2$  that is attained for  $\delta = 0$  in Eq. (16), i.e. for a constant and very weak stratification  
 498  $N^2 \equiv N_B^2$ ; the second one corresponds to the intermediate stratification given by  $\delta = \eta = 1/2$  in Eq. (18) and thus  
 499  $N^2 = N_B^2/z$  in Eq. (16). The latter one matches, as mentioned already, the stratification profile used in the results  
 500 of Section 3. The nonlinear “dispersion relation” of Fig. 8 is obtained from the continuity condition (A.8). Clearly,  
 501  $pr_0 \rightarrow 0$  as  $kr_0 \rightarrow a$ , and  $pr_0 \rightarrow \infty$  as  $kr_0 \rightarrow b$ .

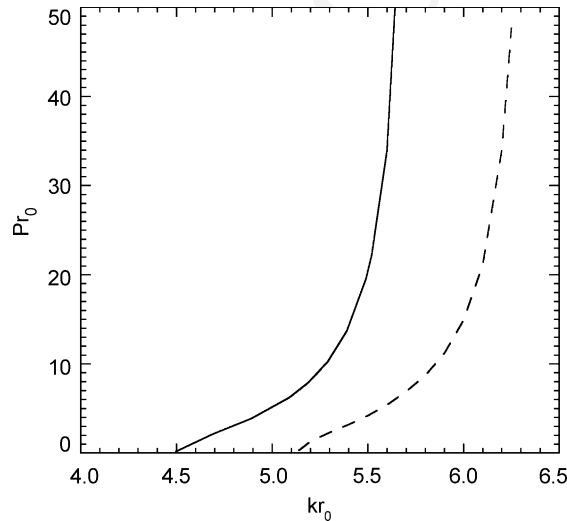


Fig. 8. Nonlinear dispersion relation for the analytic-solution parameters  $pr_0$  and  $kr_0$ , for  $\nu = 3/2$  (solid line) and  $\nu = 2$  (dashed line).

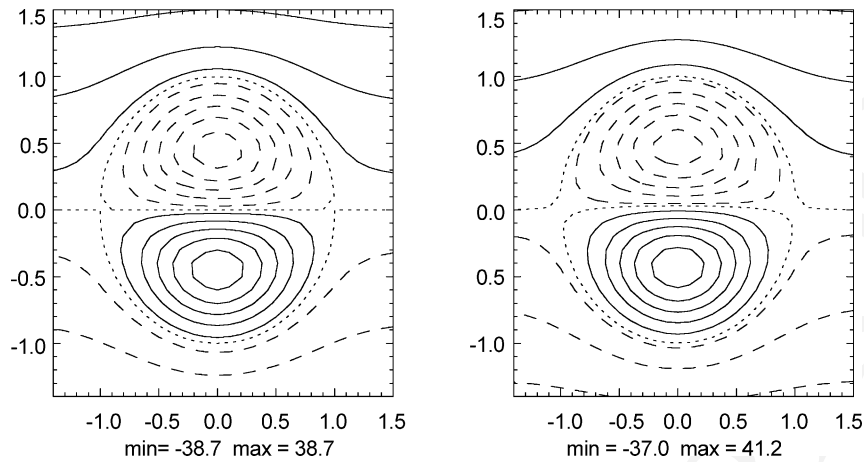


Fig. 9. The streamfunction  $\psi(x, y, z)$  of the three-dimensional analytic solutions at the sea surface  $z = 0$ : (a) the (anti)symmetric modon solution for  $\nu = 3/2$ ,  $kr_0 = 4.77$ ,  $pr_0 = 2.78$  and  $r_0 = 4.77$ ; (b) a combined modon-rider solution, in which an axisymmetric rider with amplitude  $A = 10$  and order  $\omega = 1/2$  has been added to the modon of panel (a). The range of values is symmetric in panel (a), i.e.,  $\psi_{\max} = -\psi_{\min}$ , while it is asymmetric in panel (b), with  $\psi_{\max} \cong -\psi_{\min} + A$ . Contour interval is 7.7 and the dotted line corresponds to the zero contour.

502 In Fig. 9a, the surface features of the generalized modon just described are shown for  $\nu = 3/2$ ,  $r_0 = 4.77$ ,  
 503  $kr_0 = 4.77$ , and  $pr_0 = 2.78$ . A cross-section of the modon whose surface features appear in Fig. 9a is shown in  
 504 Fig. 10. The analytical surface pattern in Fig. 9a clearly resembles that of both the barotropic (left panels) and  
 505 baroclinic (right panels) mode's dipole in Fig. 1a–c.

506 In Fig. 11 the maximum amplitudes  $\psi_{\max}/\beta r_0 k^{-2}$  of the modon at the sea surface are shown as a function of  
 507  $kr_0$  for the same two  $\nu$  values as in Fig. 8, i.e.,  $\nu = 3/2$  and 2. As  $kr_0 \rightarrow a$ ,  $\psi_{\max} \rightarrow \infty$ , while for  $kr_0 \rightarrow b$ ,  
 508  $\psi_{\max}/\beta r_0 k^{-2}$  tends to 3 for  $\nu = 3/2$  and to 4.2 for  $\nu = 2$ . Thus, the modon solution is clearly a free mode, i.e.  
 509 increasing the strength of the forcing that excites it will increase the mode's amplitude by decreasing the value of  
 510  $kr_0$  towards  $a$ .

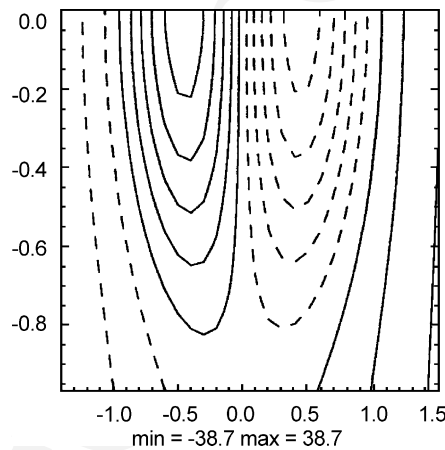


Fig. 10. Vertical cross-section  $\psi(0, y, z_*)$  of the symmetric modon solution whose plan view from above appears in Fig. 9a. The stretched vertical coordinate  $z_*$  is given by Eq. (17).

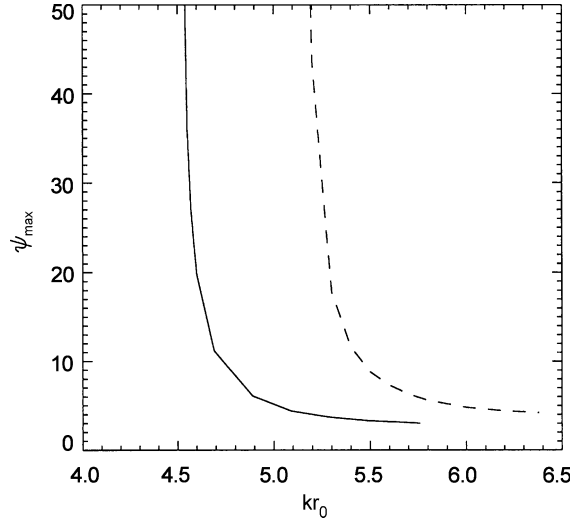


Fig. 11. The maximum amplitude of the three-dimensional modon's streamfunction,  $\psi_{\max}k^2/\beta r_0$ , as a function of  $kr_0$  for  $\nu = 3/2$  (solid line) and  $\nu = 2$  (dashed line).

511 4.2. Asymmetric solutions

512 Our numerical results show that the asymmetric steady solutions also have their most pronounced features in the  
 513 dipole region D. The free nonlinear mode found in the previous section is antisymmetric; hence it cannot explain  
 514 the numerically obtained multiple equilibria that arise due to pitchfork bifurcation (as  $\tau$  increases or  $\lambda_1$  decreases).  
 515 To obtain asymmetric free-mode solutions we add a symmetric rider to the antisymmetric dipole.

516 The equation for a 3D symmetric rider  $\psi = \psi_R(x, y, z)$  can be found from Eq. (12); it is

$$517 \quad \nabla^2 \psi_R + \frac{\partial}{\partial z} \left( \frac{1}{S} \frac{\partial \psi_R}{\partial z} \right) = \alpha \psi_R + q. \quad (25)$$

518 In the interior region  $r < r_0$ ,  $\alpha = -k^2$  and  $q \equiv E$ , say; in the exterior  $r > r_0$ ,  $\alpha = p^2$  and  $q \equiv 0$ . Since  $\psi_R$  is  
 519 symmetric, i.e. is a function of  $r$  only, Eq. (25) in spherical coordinates (21) can be written as follows:

$$520 \quad \frac{\partial^2 \psi_R}{\partial r^2} + \frac{2 + \delta/\eta}{r} \frac{\partial \psi_R}{\partial r} - \alpha \psi_R = q, \quad (26)$$

521 a particular solution  $\psi_{R(p)}$  of (26) exists only in  $r < r_0$  and is given by

$$522 \quad \psi_{R(p)} \equiv -\frac{E}{k^2} \equiv D. \quad (27)$$

523 The solution  $\psi_{R(h)} = f_{R(h)} \sin \theta$  to the homogeneous equation depends on the sign of  $\alpha$ , like that of Eq. (A.3),  
 524 and can also be found on p. 362, Eq. (9.1.53) of [52]. In the recirculating region:

$$525 \quad r < r_0, \quad \alpha = -k^2 < 0, \quad f_R(kr) = \frac{J_\omega(kr)}{r^\omega}, \quad (28)$$

526 while in the exterior region:

$$527 \quad r > r_0, \quad \alpha = p^2 > 0, \quad f_R(pr) = \frac{K_\omega(pr)}{r^\omega}, \quad (29)$$

528 the order of the Bessel functions  $J_\omega$  and  $K_\omega$  is now  $\omega = (1 + \delta/\eta)/2$ .

529 Thus the complete solution to (25) is

$$530 \quad \psi_R = A \frac{J_\omega(kr)}{r^\omega} + D, \quad r < r_0, \quad (30a)$$

$$531 \quad \psi_R = B \frac{K_\omega(pr)}{r^\omega}, \quad r > r_0, \quad (30b)$$

532 i.e. the rider tends exponentially to zero in  $r > r_0$ , and  $\omega > 1/2$  due to the values of  $\delta$  and  $\eta$  in Eq. (18).

533 The constants  $A$ ,  $B$  and  $D$  in Eqs. (30a) and (30b) are derived in Appendix A from the continuity conditions  
 534 at  $r = r_0$ . It follows from Eqs. (A.9)–(A.11) that  $B$  and  $D$  are proportional to  $A$ ; thus  $A$  is a free parameter and  
 535 determines the amplitude of the rider. For the case of constant stratification— $\delta = 0$ ,  $v = 0$  and  $N \equiv N_B$ —Kizner  
 536 [53] found a different symmetric rider that is characterized by its vorticity being continuous across the streamline  
 537  $r = r_0$ .

538 The superposition of the modon and the rider is a free asymmetric nonlinear mode. We interpret the asymmetric  
 539 numerical dipoles that arise from the pitchfork bifurcation of the antisymmetric steady state as follows: the eastward  
 540 extension of the separated western boundary currents excites the modon–rider free mode. For moderate jet strength,  
 541 the rider’s amplitude is weak relative to that of the antisymmetric modon and the solution is close to antisymmetry.  
 542 As the jet intensifies due to an increase in the wind stress  $\tau$ , the relative amplitude of the rider increases and the  
 543 solution becomes more asymmetric.

544 We noted already in the previous section that the surface features of the modon solution (A.6a) and (A.6b), as  
 545 shown in Fig. 9a, resemble quite well with the features of the baroclinic mode in the dipole region of the nearly  
 546 symmetric numerical solutions in Fig. 1a–c. An asymmetric modon–rider combination is shown in Fig. 9b, where a  
 547 rider with  $A = 10$  and  $\omega = 1/2$  has been added to the antisymmetric modon of Fig. 9a. The deviation from symmetry  
 548 of this solution is clearly observed in both the relative sizes of the two recirculating vortices—the cyclonic one is  
 549 smaller than the anticyclonic one—and their relative amplitude, with  $\psi_{\max} > |\psi_{\min}|$ .

550 Both the surface features and amplitude of the modon–rider solution shown in Fig. 9b resemble those of the  
 551 baroclinic mode of the asymmetric numerical dipole shown in Fig. 1d. More precisely, the surface features of the  
 552 numerical dipole are given by  $\psi(x, y, 0) = \psi_0(x, y) + \phi_1(0)\psi_1(x, y)$  (not shown); it is the later that should be  
 553 directly compared with Fig. 9b. This interpretation of the numerical solutions in terms of the analytical ones is  
 554 clearly heuristic, since the rider is passive in the free-mode solution, i.e. the conservative dynamics of the combined  
 555 modon–rider system does not depend on the rider’s amplitude  $A$ , unlike in the full, forced-dissipative system  
 556 (1a)–(4).

## 557 5. Comparison of analytical and numerical results

558 We are interested now in comparing the key properties of the analytical solutions—symmetric and asymmetric,  
 559 as obtained in Sections 4.1 and 4.2, respectively—with the corresponding properties of the numerical solutions’  
 560 dipole region D. Greatbatch [38] carried out such a comparison between Stern’s [39] modon and the recirculating  
 561 subgyres of the multi-layer eddy-resolving models of Böning [54] and Holland and Schmitz [55]. He found that the  
 562 match was imperfect, but reasonable, in the dependence of the subgyres’ longitudinal (east–west) and latitudinal  
 563 (north–south) extent on the inertial length scale  $(V/\beta)^{1/2}$  (in our notation here), as long as he concentrated on  
 564 Böning’s steady-state solutions. The eastward jet’s penetration depth, however, was much larger than that sug-  
 565 gested by the steady-state experiments—and did not depend in a simple way on the inertial length scale—for those  
 566 numerical experiments in which only a statistical equilibrium was obtained. This was the case for some of Böning’s  
 567 and all of Holland and Schmitz’s experiments.

568 Greatbatch [38] attributed the latter discrepancy to the fact that, in the fully turbulent solutions, PV homogenization  
 569 [7, Section 3.8; 56] occurs inside the recirculation zone. Thus the linear relation between PV and streamfunction  
 570 tends to hold there with a proportionality constant  $\alpha = 0$ , rather than with  $\alpha < 0$ , as it does for the interior of  
 571 Stern’s modon or of our three-dimensional generalization thereof. We shall restrict, therefore, our comparisons  
 572 to the steady-state solutions of our QG model, but extend them, on the other hand, to steady-state solutions of  
 573 a reduced-gravity shallow-water model (JJG; [14]) as well. The relevance of the multiple equilibria and periodic  
 574 solutions of such simple models to multi-layer models at higher Reynolds number has been discussed recently by  
 575 Berloff and McWilliams [31] and Simonnet et al. [32,33]. We shall comment further on this matter in Section 6.2.

576 *5.1. Comparison with the numerical QG results*

577 We compare first the antisymmetric analytical solutions of Section 4.1 with the corresponding numerical QG  
 578 solutions of Section 3.2. The procedure is as follows. Conceptually, the stratification profile  $N = N(z)$  determines  
 579 the vertical modes  $\phi_k = \phi_k(z)$  and associated eigenvalues  $\lambda_k$ ,  $k = 0, 1$ , in Eq. (5). In practice, for the numerical QG  
 580 model (7) we use the value  $\xi_{111} = 1.8$  for the only triple interaction coefficient that is not equal to 0 or 1 and  $\phi_1(0) =$   
 581 4, while  $\phi_0(z) \equiv 1$ ; furthermore, it is customary to set  $\phi_1(1) = -1/2$  (see Table 1). These values for  $\xi_{111}$  and  $\phi_1(0)$   
 582 correspond to the North Atlantic’s stratification (see [21,24]). In our numerical model,  $1/\lambda_1$  is a control parameter.

583 The values of the triple interaction coefficients and the boundary values of the eigenmodes—along with those of  
 584 the control parameters  $1/\lambda_1$  and  $\tau$ —determine the numerical solutions of Eq. (7) with boundary conditions (2a)–(3)  
 585 and diagnostic relations (8). Three scalars that capture key characteristics of the numerical solutions in the dipole  
 586 region D are  $\psi_{\max}$ , the slope  $\alpha$  of the linear regression relation between PV and the streamfunction  $\psi$ , and the radial  
 587 scale  $R_d$  (see Table 3). We shall describe below how  $\alpha$  is obtained in greater detail.

588 The analytical solution (22a) and (22b) that best matches a given numerical solution is determined as follows. To  
 589 obtain the analytical stratification profile (16), we need the values of  $N_B$  and  $\delta$ . These are computed by trial-and-error,  
 590 solving Eqs. (5) and (8) with different pairs  $(N_B, \delta)$  substituted into  $S = S(z)$  until a good match is obtained for  
 591  $\xi_{111}$ ,  $\phi_1(0)$  and  $1/\lambda_1$ . It turns out that  $\delta = 1/2$  and hence  $\nu = 2$  are very good matches for the values  $\xi_{111}$  and  $\phi_1(0)$   
 592 in Table 1, over the entire range of  $1/\lambda_1$  used in Section 3. The values of  $N_B$  we obtain are between  $1.2 \times 10^{-3}$   
 593 and  $2.7 \times 10^{-3}$  for  $3/5 \leq 1/\lambda_1 \leq 7/5$ . Both the  $\delta$ -value and the range of  $N_B$  are close to those that can be directly  
 594 inferred from North Atlantic observations.

595 Having thus obtained  $N_B$  and  $\delta$ ,  $k$  is selected to yield  $-k^2 = \alpha$  and the analytical radius  $r_0$  is determined by  
 596 matching, at the surface  $z = 0$ , the analytical  $\psi_{\max}^{(a)} = \psi_{\max}(k, r_0)$  to the numerical one. Next, the scale  $R_d^{(a)}$  of the  
 597 analytical dipole is defined as the east–west distance between either pole and the point on the zero streamline due  
 598 east of it. Finally, the analytical  $R_d^{(a)}$  so defined (last column of Table 3) is compared with the numerical value  $R_d$   
 599 (in the preceding column).

600 The value of  $\alpha$  in the numerical solution is basically found by examining the functional relation (12) in the dipole  
 601 region. Due to the 3D structure of our analytical dipole solution (see Fig. 10),  $\alpha$  changes with depth: for any  $r \neq 0$ ,  
 602  $\alpha = -k^2 < 0$  in the model’s upper ocean inside our generalized modon, while in the lower ocean  $\alpha = p^2 > 0$   
 603 outside the modon. Thus, it is convenient to evaluate  $\alpha$  inside the dipole at the equivalent-barotropic level  $z_0$ , where  
 604  $\phi_1(z_0) = 0$ . At this level only the barotropic mode is present in (12), and thus

605 
$$\nabla^2 \psi_0 + \beta y = \alpha \psi_0 \tag{31}$$

606 has to hold there.

607 Given (31), we find  $\alpha$  by plotting  $\nabla^2 \psi_0 + \beta \psi$  as a function of  $\psi_0$  for each point within the circle of radius  $R_d/2$   
 608 around the center of the numerical dipole (see the first paragraph of Section 4.1), and fit a straight line to these points  
 609 by least squares. The slope of this line is  $\alpha$  and the scatter of points about it is strikingly small (not shown here for

610 the QG model, but see Section 5.2 for the appropriate plot based on the shallow-water model). The maximum of  
 611 the function  $|\psi_0(x, y) + \phi_1(0)\psi_1(x, y)|$  within the numerical dipole then yields  $\psi_{\max}$ . Table 3 displays  $\alpha$  and  $\psi_{\max}$   
 612 for the different numerical experiments, as identified by the values of  $1/\lambda_1$  and  $\tau$  used therein. In all cases  $\alpha < 0$ ,  
 613 and so we can use  $\psi_{\max}$  and the modon's scale parameter  $k = \sqrt{-\alpha}$  to find  $r_0$  as a function of  $\nu$  from Eq. (A.6a).

614 In Table 3,  $R_d^{(a)}$  is given for  $\delta = \eta = 1/2$  and  $\nu = 2$ . Comparing this analytical value  $R_d^{(a)}$  with the numerical  
 615 value  $R_d$  (Table 3), we find that the two agree quite well in all cases. The difference is at most about 5% for all the  
 616 symmetric steady states computed; the largest difference occurs close to the pitchfork bifurcation point.

617 For all the numerical experiments and values of  $\nu$ , the best fit value of  $kr_0$  is  $5.6 \pm 0.1$ . Hence, the scale  $R_d$  of the  
 618 numerical dipole does equal approximately  $r_0 \cong 5.6/k = 5.6/\sqrt{-\alpha}$ ; it is thus determined by the linear functional  
 619 dependence between the PV and the streamfunction that prevails within the dipole.

620 It follows that—by a fairly broad set of quantitative measures, as well as by its overall qualitative similarity in  
 621 surface flow pattern—the analytical free-mode solution of Section 4.1 approximates well the steady state, forced-  
 622 dissipative solutions of Section 3.2 in the dipole region D. The numerical results on the mesoscale dipole's flow  
 623 pattern may thus be interpreted as the result of a free-mode solution's being resonantly excited by the seaward exten-  
 624 sion of the western boundary currents. The eastward jet's seaward profile has, indeed, a linear functional dependence  
 625 between  $Q$  and  $\psi$ —as given by (12), with  $\alpha < 0$  (not shown)—which is entirely consistent with this explanation.

626 Pierrehumbert and Malguzzi [43] introduced a solvability condition to select free-mode solutions of the barotropic  
 627 counterpart of Eq. (11) that approximate well with the solution of a barotropic QG problem with weak forcing and  
 628 dissipation. Given the good match between our 3D free mode and the numerical solutions of Section 3, we expect  
 629 a 3D generalization of their solvability condition to hold in the present situation. The basic idea of their condition  
 630 is that not every solution of the inviscid steady-state barotropic vorticity equation can approximate well with that  
 631 of the barotropic or equivalent-barotropic vorticity equation subject to weak forcing and dissipation. In fact, the  
 632 solutions to the former form a continuous, highly degenerate family of solutions, while the inclusion of forcing and  
 633 dissipation, however, weak, removes much of this degeneracy and can lead to a discrete set of solutions [45].

634 In the barotropic, two-dimensional (2D) case, Pierrehumbert and Malguzzi [43] explored two distinct cases, for  
 635 closed and open streamlines. For a closed streamline, the Lagrangian time average of the net forcing obtained by  
 636 following a fluid particle along the streamline must vanish identically. Otherwise, no matter how small the net  
 637 forcing, it would have a large effect on the solution, as the fluid particle keeps repeating its motion over and over  
 638 again. For an open streamline, a weaker condition suffices, i.e. the Lagrangian time average must merely be small,  
 639 as a fluid particle will only traverse once the region where the approximation should apply. This weaker condition  
 640 is still nontrivial for an open streamline of infinite length.

641 In our case, we compare the analytical inviscid solution with the corresponding numerical solution in the dipole  
 642 region D, within the area where the nonlinear terms are balanced by the  $\beta$ -term. This area is mainly in the central  
 643 and eastern part of the recirculation region, as shown in Section 3.3 and Figs. 6 and 7. In the western part of D  
 644 the friction term cannot be neglected and so the inviscid solution is not appropriate near the western boundary.  
 645 Furthermore, we expect the solvability conditions [43] for both open and closed streamlines to apply roughly at the  
 646 equivalent-barotropic level  $z_0$ . This is certainly the case for the open streamlines in the eastern part of D, since they  
 647 have finite length. It is approximately the case for the small-diameter closed streamlines in the central part of D, for  
 648 which we have not been able to derive the exact generalization to Eqs. (7) and (11) of the appropriate condition of  
 649 Pierrehumbert and Malguzzi [43].

## 650 5.2. Comparison with shallow-water model results

651 To corroborate further the good description provided by the analytical solutions for steady-state recirculating  
 652 flows in a wind-driven rectangular ocean basin, we study in this section the relation between PV and streamfunction

653 for the symmetric and asymmetric steady solutions of a reduced-gravity, 1.5-layer, shallow-water model. The model  
 654 follows the one used by JJG and Speich et al. [14]. The rectangular domain has an east–west extent of 1000 km  
 655 and north–south extent of 2000 km. The model’s fixed parameter values differ in certain details from those given in  
 656 Table 1 here; they are given in Table 1 of JJG. The system of equations (21) of JJG was nondimensionalized using  
 657 the characteristic scales given in Table 1 here, to be consistent with the QG model above.

658 The model equations are solved on a staggered C-grid with a mesh size  $L\Delta x = L\Delta y = 12.5$  km and a time step  
 659  $T\Delta t = 600$  s, using no-slip boundary conditions. More details regarding the model can be found in JJG and [57].  
 660 The horizontal resolution used here is larger than in these two previous studies, to match approximately with that of  
 661 the QG model (see Section 2:  $L\Delta x = L\Delta y = 10$  km for the QG model). The system’s behavior is determined by  $\alpha_\tau$   
 662 and  $\alpha_A$ , the coefficients that control the strength of the external wind forcing and the lateral viscosity, respectively;  
 663 the nonlinearity increases with increasing  $\alpha_\tau$  and decreasing  $\alpha_A$ .

664 The streamfunction  $\psi$  is obtained from the Cartesian velocity components of the shallow-water model’s active  
 665 upper layer, subject to the appropriate boundary conditions. The PV is given in this case by

$$666 \quad \tilde{Q} \equiv \nabla^2\psi + \beta y - \lambda^2\psi. \quad (32)$$

667 The Rossby radius of deformation given in dimensional units by  $L\lambda^{-1} = (g'H)^{1/2}/f$  is equal to about 80 km in  
 668 the JJG model version used here. This corresponds to  $\lambda = 0.63$  in nondimensional units, and is meant to match  
 669  $\lambda_1$  in the QG model. The stratification in this reduced-gravity, 1.5-layer model cannot be defined by a continuous  
 670 function  $S = S(z)$ , as in our QG model (7). For the purposes of a match with the analytical solution, we select a  
 671 reasonably weak stratification of  $\delta \cong 0.1$  and hence  $\nu \cong 1.65$ .

672 We summarize briefly the JJG model’s changes in behavior, for fixed  $\alpha_A$ , as  $\alpha_\tau$  is increased. These are captured  
 673 by its bifurcation diagram for the normalized transport difference (TD) between the two gyres, as a function of  $\alpha_\tau$   
 674 (not shown here, but see JJG and [14] for closely related bifurcation diagrams).

675 Following Chang et al. [25], TD is defined here as

$$676 \quad \text{TD} = \frac{|\psi_{\text{po}}| - |\psi_{\text{tr}}|}{\max|\psi|}, \quad (33)$$

677  $\psi_{\text{po}}$  and  $\psi_{\text{tr}}$  are the maximum transports of the subpolar and subtropical gyres, respectively, with  $\psi_{\text{po}} < 0 < \psi_{\text{tr}}$ ,  
 678 and  $\max|\psi|$  the larger of  $|\psi_{\text{po}}|$  and  $|\psi_{\text{tr}}|$ . An antisymmetric flow pattern, with subtropical and subpolar gyres of  
 679 equal strength, corresponds to  $\text{TD} = 0$ , while a stronger subpolar gyre corresponds to  $\text{TD} > 0$  and a stronger  
 680 subtropical gyre to  $\text{TD} < 0$ .

681 For very low  $\alpha_\tau$ , the double-gyre circulation in this model is antisymmetric about the mid-axis of the basin, with  
 682 zero TD, as it is in the QG model. Upon increasing  $\alpha_\tau$ , the subpolar gyre gains strength ( $\text{TD} > 0$ ), and leads to  
 683 a positive branch, for which the northward western boundary current detaches later and the subtropical gyre has a  
 684 larger area, although it is weaker (see JJG and [14]); the TD increases with increasing  $\alpha_\tau$  values along this branch.

685 As the parameter  $\alpha_\tau$  increases further, a first bifurcation to multiple steady states occurs, i.e. a positive and a  
 686 negative branch coexist and are both stable. The negative branch has a stronger subtropical gyre, which increases  
 687 in strength faster with  $\alpha_\tau$  than the subpolar gyre along this branch, so that  $d(\text{TD})/d\alpha_\tau < 0$  along it. The bifurcation  
 688 giving rise in this model to the asymmetric multiple equilibria is of the perturbed pitchfork type; the perturbation  
 689 with respect to the QG model is due to the lack of mid-basin symmetry of the shallow-water model’s free surface.

690 Both steady-state branches then lose their stability to periodic solutions at slightly different  $\alpha_\tau$  values, in keeping  
 691 with the overall lack of symmetry between the positive and the negative branch. The two bifurcations that lead to the  
 692 periodic motion are both of Hopf type, as were the two mutually symmetric ones in the QG model. Upon increasing  
 693 the wind stress further, the periodic solutions give way to aperiodic ones.

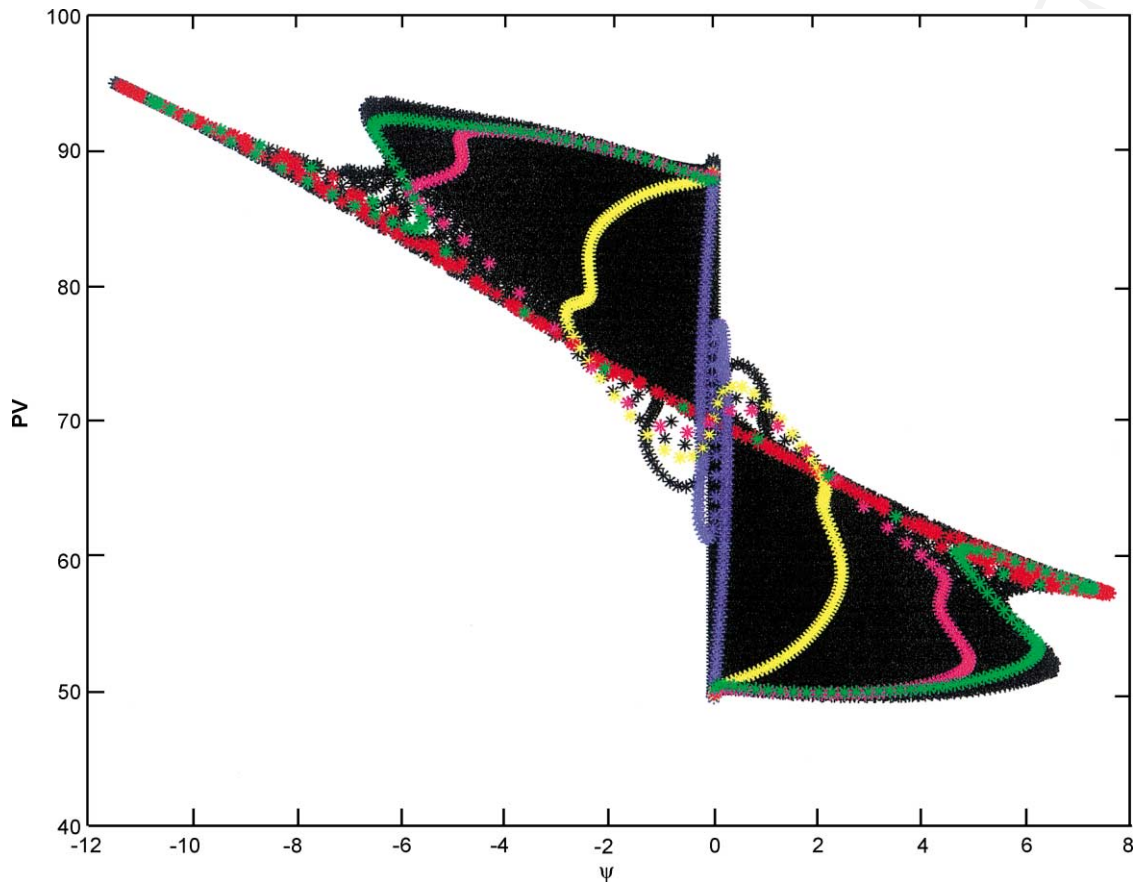


Fig. 12. Scatter plot of PV vs. streamfunction in JjG's shallow-water model, for the entire basin and  $\alpha_\tau = 0.62$ :  $(\tilde{Q}, \psi)$  pairs taken from the recirculation zone are red and those from the Sverdrup region are black, while the blue, yellow, purple and green points correspond to grid points at  $0\Delta x$ ,  $2\Delta x$ ,  $4\Delta x$  and  $10\Delta x$  from the western boundary; the seaward limit of the Munk layer is at  $2\Delta x$  (yellow) and that of the inertial layer at  $4\Delta x$  (purple).

694 Irrespective of the flow regime, i.e., symmetric steady, asymmetric steady, periodic or aperiodic, three major  
 695 spatial patterns can be identified in the model's rectangular basin. They resemble very well with those described  
 696 in Section 3.3 for the QG model. The dynamically different regions are noticeable on scatter plots of  $\tilde{Q}$  vs.  $\psi$   
 697 (Fig. 12).

698 For the dipole region, all the points (red in Fig. 12) fall very close to a straight line with a negative slope (Fig. 13).  
 699 Points outside the dipole region in Fig. 12 are spread over a larger area of the  $\tilde{Q}$ - $\psi$  plane: the Sverdrup region  
 700 (black) covers the two large curvilinear triangles between the dipole region and the blue nearly straight line along  
 701 the ordinate of the scatter plot at  $\psi = 0$ ; these two black triangles, like the entire scatter plot, are mirror symmetric  
 702 in the plot's origin  $(\psi, \tilde{Q}) = (0, 0)$ . The seaward boundary of the frictional layer is the yellow curve and that of the  
 703 inertial layer is the purple one.

704 We investigate now in detail the relation between PV and  $\psi$  in the dipole region for both antisymmetric and  
 705 asymmetric solutions. The points in the dipole region fall on a straight line, for all cases investigated. The slope  
 706  $\alpha$  of this line for some of the cases studied is given in Table 4 and is found to decrease in absolute value as the  
 707 wind-stress forcing increases.

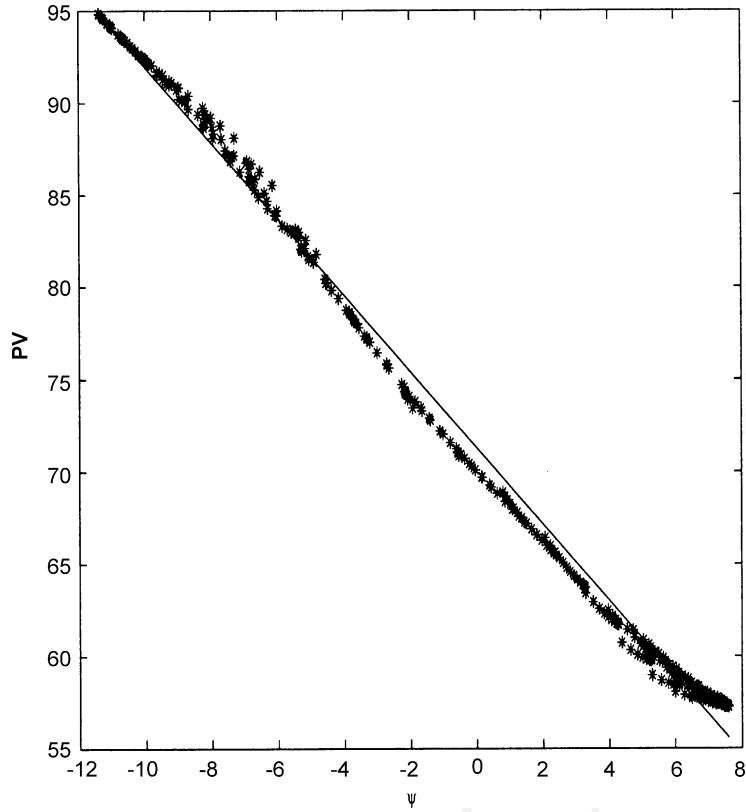


Fig. 13. Scatter plot of PV vs. streamfunction, restricted to the JJG model's dipole region, for  $\alpha_\tau = 0.62$ ; the regression coefficient is  $\rho = -0.9977$ .

Table 4

Characteristic parameters of the least-square dipole for some values of  $\alpha_\tau$  that yield symmetric ( $TD = 0$ ) and asymmetric ( $TD \neq 0$ ) steady solutions in the JJG model, for  $\lambda = 0.63$ ; the value of  $R_d^{(a)}$  corresponds to  $\nu = 1.65^a$

$\alpha_\tau$	$\alpha$	$\max \psi $	$ TD $	$R_d$	$R_d^{(a)}$	$\rho$
0.41	-2.51	4.62	0	2.84	3.2	-0.9985
0.43	-2.42	5.03	0	2.89	3.3	-0.9984
0.47	-2.28	5.91	0	3.04	3.3	-0.9987
0.52	-2.18	7.81	0.17	3.20	3.3	-0.9984
0.54	-2.15	8.48	0.18	3.39	3.2	-0.9982
0.55	-2.13	8.84	0.21	3.34	3.2	-0.9975
0.56	-2.10	9.22	0.23	3.41	3.15	-0.9980
0.58	-2.09	9.98	0.27	3.43	3.15	-0.9981
0.60	-2.09	10.72	0.30	3.51	3.14	-0.9979
0.62	-2.06	11.48	0.33	3.61	3.14	-0.9977
0.80	-1.76	15.64	0.32	3.84	3.45	-0.9908
0.82	-1.76	16.20	0.33	3.81	3.44	-0.9908
0.84	-1.74	16.75	0.34	3.81	3.44	-0.9916

<sup>a</sup> The value of  $\max|\psi|$  is the larger of  $|\psi_{p0}|$  and  $|\psi_{tr}|$ ; see text for details. The regression coefficient  $\rho$  for the scatter of numerically obtained  $(\bar{Q}, \psi)$  pairs around the least-square straight line with slope  $\alpha$  is given in the last column.

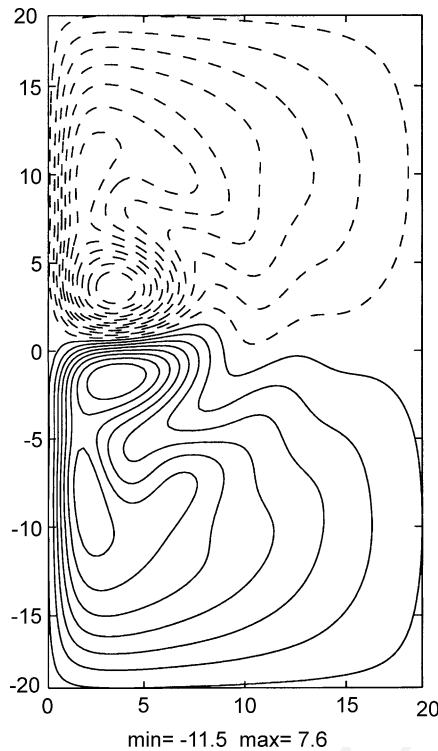


Fig. 14. Streamfunction of the JJG model for the entire basin and  $\alpha_\tau = 0.62$ .

708 The scale of the dipole  $R_d$ , defined in the same way as for the QG model (see Section 3.2), is also shown in the  
 709 table. For the asymmetric cases, since the two vortices possess different strengths and sizes, the average of the two  
 710 is chosen. For both the antisymmetric and asymmetric steady solutions given in Table 4, the numerical model's  
 711 scale  $R_d$  is within a relative error of less than 15% of the proposed analytical model's scale  $R_d^{(a)}$ . The agreement  
 712 between the numerical and analytical solution is quite good. This can also be seen from the very high values of the  
 713 regression coefficient  $\rho$  in the last column of Table 4; the scatter of the numerically obtained  $(\tilde{Q}, \psi)$  points around  
 714 the least-square fit line is quite minimal.

715 As proposed in Section 4.2 for the QG model, it is observed that the dipole region of all asymmetric steady solutions  
 716 of the shallow-water model can be obtained by superposing a symmetric monopole upon an antisymmetric dipole  
 717 as well. The streamfunction for the entire basin is plotted in Fig. 14 for the asymmetric case with  $\alpha_\tau = 0.62$ , which  
 718 yields a fairly strong subpolar gyre. A zoom-in of the recirculation zone of the JJG model's flow pattern in Fig.  
 719 14 is shown as Fig. 15a. This numerically obtained streamfunction field is decomposed into its antisymmetric part  
 720 (Fig. 15b) and its symmetric part (Fig. 15c). The major aspects of this decomposition resemble well the surface  
 721 features of the asymmetric analytic solution shown in Fig. 9b, with its antisymmetric part (Fig. 15b) bearing the  
 722 dipole features of Fig. 9a and its symmetric part (Fig. 15c) bearing, even more surprisingly, the monopole features  
 723 of the corresponding analytic rider (not shown).

724 The amplitudes of the best fit antisymmetric dipole and symmetric monopole for a few values of the wind-stress  
 725 forcing are given in Table 5:  $|\psi_{di}|$  is the maximum of the analytical solution given by Eq. (22a) that best fits the  
 726 antisymmetric part of the numerical solution, as defined in the caption of Fig. 15b, while  $\psi_{mono}$  the maximum of  
 727 the analytical solution of Eq. (30a) that best fits the symmetric part of the numerical solution, as defined in the

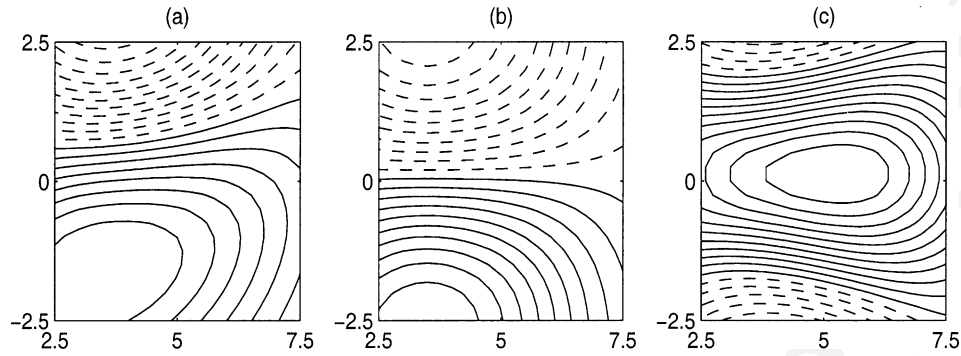


Fig. 15. Odd–even decomposition of the numerical solution’s streamfunction  $\psi = \psi_a(x, y)$ : (a) dipole region of the asymmetric numerical JIG solution for  $\alpha_\tau = 0.62$  (blow-up of Fig. 14); (b) the antisymmetric part  $\psi_b$  of the streamfunction field in panel (a),  $\psi_b(x, y) = [\psi_a(x, y) - \psi_a(x, -y)]/2$ ; (c) the symmetric part  $\psi_c$  of the streamfunction in panel (a),  $\psi_c(x, y) = [\psi_a(x, y) + \psi_a(x, -y)]/2$ .

Table 5

Amplitudes of the antisymmetric dipole and symmetric monopole for some  $\alpha_\tau$  values that yield asymmetric steady solutions with a strong subpolar gyre for  $\lambda = 0.63$ ; see text for the exact definitions of  $\psi_{di}$  and  $\psi_{mono}$

$\alpha_\tau$	$ \psi_{di} $	$\psi_{mono}$
0.52	6.62	0.79
0.54	7.03	1.18
0.55	7.22	1.42
0.56	7.41	1.69
0.58	7.74	2.27
0.60	8.02	2.86
0.62	8.28	3.42

728 caption of Fig. 15c. The strength of the antisymmetric dipole increases slowly with  $\alpha_\tau$ , while that of the symmetric  
 729 monopole increases rapidly away from the initial point of the perturbed pitchfork bifurcation, which occurs between  
 730  $\alpha_\tau = 0.47$  and 0.52 (see Table 4). This suggests that the system’s stability decreases and its nonlinearity increases  
 731 as the rider becomes stronger.

## 732 6. Concluding remarks

### 733 6.1. Summary

734 We studied the problem of low-frequency variability in the double-gyre circulation induced by the wind stress in  
 735 a rectangular mid-latitude basin, using a QG two-mode model. This numerical QG study was complemented by the  
 736 analytical study of free-mode dipole and monopole solutions of the PV equation in a continuously stratified ocean,  
 737 and by a supporting numerical study of a shallow-water model for the double-gyre circulation.

738 The numerical solutions of the QG model were examined as a function of two key parameters—the wind-stress  
 739 intensity  $\tau$  and the Rossby radius of deformation  $L_R$ —out of nine independent parameters which govern the problem.  
 740 For a time-constant wind-stress forcing that is antisymmetric about the rectangular basin’s zonal axis of symmetry,  
 741 we found symmetric and asymmetric multiple equilibria (Fig. 1), as well as periodic (Fig. 4) and chaotic (Fig. 5)  
 742 solutions.

743 These results support and extend those obtained for both shallow-water and QG models in a number of recent  
744 papers [10–12,14,18,25,32,33]. Several among these, in particular [14,32,33], emphasized that the overall bifurcation  
745 structure of the problem does not depend on the exact governing equations, QG or shallow-water, the number of  
746 layers, the parameter being varied and those being kept fixed, or the numerical resolution.

747 We clarified further the problem’s bifurcation structure in the following sense. For  $1/\lambda_1 > 1$ , transition to chaos  
748 from a unique (anti)symmetric solution happens via a pitchfork bifurcation (Fig. 2) followed by a Hopf bifurcation,  
749 while for  $1/\lambda_1 < 1$  the pitchfork bifurcation stage is skipped. This result is summarized in the “catastrophe diagram”  
750 of Fig. 3. Two successive Hopf bifurcations excite first a dominant period of 10.4 years and, as  $\tau$  increases further,  
751 a second period of 1.7 years. The decadal period of the first Hopf bifurcation is associated with the baroclinic  
752 character of the associated linear instability (see Fig. 4).

753 The numerical solutions are characterized—independent of their variability and degree of symmetry—by three  
754 types of spatially circumscribed flow patterns: (1) a basin-scale double-gyre circulation, (2) a north- and a southward  
755 flowing western boundary current and, near the confluence of the two, (3) a strong dipole. Our highly idealized QG  
756 model captures therewith, in spite of its many simplifying assumptions, key features of the mid-latitude oceans’  
757 wind-driven circulation. We have denoted the three subdomains which these characteristic flow patterns occupy by  
758 G, W and D, respectively; G refers to the complement within the rectangular domain of the union of D and W.

759 The physical nature of the flow in each subdomain was examined by considering the relative importance of  
760 the terms in the PV equations (1a)–(1e) that governs our model. As in the world’s mid-latitude ocean basins, the  
761 double-gyre region G is governed by the Sverdrup relation, with the curl of the wind stress balanced by the  $\beta$ -effect.  
762 The flow in region G is relatively weak when compared to both D and W, and much stronger in the first baroclinic  
763 mode  $k = 1$  than in the barotropic mode  $k = 0$  (see Fig. 1). In the boundary region W, the  $\beta$ -term is balanced by  
764 horizontal friction closest to the coast, and by nonlinear advection further out to sea. Thus, a thinner frictional layer  
765 is embedded in a slightly wider inertial boundary layer.

766 The dipole region D exhibits prominent recirculation in both the barotropic and baroclinic modes. The  $\beta$ -term  
767 tends to propagate the dipole westward. This linear tendency is balanced by a nonlinear eastward-propagation  
768 tendency, due to mutual advection of the dipole’s two eddies. Nonlinear interaction between the barotropic and  
769 baroclinic modes is prominent in this region (see Figs. 6 and 7).

770 The key role of the dipole region in the double-gyre problem’s multiplicity and variability of solutions had already  
771 been pointed out by JJG and Jiang and Ghil [58]. We concentrated therefore on casting further light on this region  
772 by obtaining and studying analytical solutions that exhibit flow patterns resembling the symmetric or asymmetric  
773 character of the flow there.

774 Exact solutions of the vorticity or PV equation in two dimensions, in the absence of forcing and dissipation, are  
775 fairly well known [35,39,40]. These solutions are based on the steady-state form of the inviscid governing equation,  
776 which imposes a functional relationship between the vorticity and the streamfunction. While actual oceanic flows  
777 are forced and dissipative, as in the full numerical QG model we have been using, a straight line  $Q = \alpha\psi$  is often  
778 found to approximate well with the observed scatter plot of the two quantities.

779 A number of attempts to generalize Stern’s modon to multi-layer flows were undertaken by Greatbatch [37,38] and  
780 Marshall and co-workers [29,47]. Berestov [50] and Kizner [53] also obtained truly 3D, closed-form modon-type  
781 solutions for the case of constant stratification. We generalize this work by obtaining exact 3D, free-mode solu-  
782 tions for a continuously stratified QG model ocean, in the presence of variable stratification. These solutions are  
783 characterized by  $\alpha = -k^2 < 0$  inside the recirculating region and  $\alpha = p^2 > 0$  outside it (see Figs. 9a and 10).

784 A close relation between our analytic modon-type solution of Section 4 and our steady-state numerical solutions  
785 of Section 3 is found in Section 5 for the parameter values  $\delta = \eta = 1/2$ ,  $\nu = 2$  that correspond to the typical  
786 stratification of the North Atlantic basin. This good match is essentially due to the fact that, in our rectangular  
787 domain’s dipole region, the functional dependence between  $Q$  and the streamfunction  $\psi$  is almost linear, with

788  $\alpha < 0$  (see Table 3). After least-square fitting  $\alpha$  and the maximum amplitude  $\psi_{\max}$  of the analytical modon's  
789 streamfunction (see Fig. 9a) to that of the numerical dipole (see Fig. 1a–c), we find excellent agreement between  
790 their respective radial scales  $R_d^{(a)}$  and  $R_d$ . The common horizontal scale of the analytical modon and numerical  
791 dipole in the upper ocean is given by  $r_0 \cong 5.6/k = 5.6/\sqrt{-\alpha}$ , with a relative error of less than 3%. We also found  
792 the negative slope  $\alpha$  of the least-square fit to decrease in absolute value as the wind-stress intensity  $\tau$  that generates  
793 the numerical solution increases (see again Table 3).

794 Asymmetric analytical solutions were obtained by adding a symmetric, 3D, monopole rider to the antisymmetric  
795 dipole. These solutions (Fig. 9b) resemble the asymmetric numerical dipoles in region D that are part of the  
796 steady-state numerical solutions obtained through pitchfork bifurcation (Fig. 1d).

797 The good match between the antisymmetric and asymmetric numerical solutions, on the one hand, and the  
798 corresponding analytic solutions on the other, encouraged us to broaden the comparison and introduce yet another  
799 type of model into it. The model we chose is the primitive-equation, shallow-water model of JJG which incorporates  
800 certain features of current ocean general circulation models (GCMs) not captured by our QG model.

801 For this model, too, we find good agreement between the analytical radial scale  $R_d^{(a)}$  and the numerical one  $R_d$ .  
802 The common horizontal scale of the analytical modon and numerical dipole in this case is given by  $kr_0 \cong 5.3$ , with a  
803 relative error of less than 6%. Moreover, the JJG model's scatter around the regression line for PV vs. streamfunction  
804 (Fig. 13) is very small in the dipole region, for both antisymmetric and asymmetric steady-state solutions (see  
805 Table 4). In fact, we can match very well the numerical model's increasingly asymmetric dipole as the wind-stress  
806 intensity, denoted here by  $\alpha_\tau$ , increases; this match requires a slight increase in the amplitude of the analytical  
807 dipole, accompanied by a pronounced increase in the amplitude of the monopole rider (see Table 5 and Fig. 15).

808 The slope  $\alpha$  of the least-square straight line obtained from the scatter plot of PV vs.  $\psi$  in the dipole region  
809 decreases markedly in absolute value as the wind stress increases and the solutions become therewith more skewed  
810 and nonlinear (Table 4). It is also clear that in the rest of the primitive-equation model's rectangular domain, the scatter  
811 of the points  $(\psi, \tilde{Q})$  obeys certain interesting and yet-to-be elucidated constraints; this scatter occupies a substantial  
812 area of the two-dimensional surface available to it, between the positive and negative extreme of the streamfunction  
813 and the positive maximum and minimum of PV (Fig. 12), rather than falling essentially along a straight line.

814 The exact dynamical connection between the analytic and numerical solutions remains an open question. The  
815 former are free modes of the steady state, conservative PV equation (12), while the latter are solutions of the full,  
816 forced-dissipative system (1a)–(4). Free modes and Hamiltonian dynamics have been playing an increasing role in  
817 explaining fluid-dynamics phenomena in general [59] and in atmospheric applications in particular [41,42]. Still,  
818 the specifics of each such application are not self-evident and we return to this matter in the discussion below.

## 819 6.2. Discussion

820 The main purpose of the present paper was to study certain fundamental aspects of the mid-latitude ocean's  
821 wind-driven circulation. This was done by using two numerical and one analytic model, all of which are highly  
822 idealized. Still, there are some striking similarities, at least in the qualitative sense, between our model results and  
823 observed features of the world oceans' circulation, as well as with fairly detailed and presumably realistic model  
824 simulations of these features. We point out one such similarity and also one fundamental difference between our  
825 idealized model results and certain properties of the world oceans' recirculation zones. The latter difference is, in  
826 a sense, quite enlightening and points the way to future research.

827 Chao et al. [60] used a high-resolution ocean GCM to simulate the North Atlantic basin's circulation. In this  
828 simulation, the Gulf Stream separates at Cape Hatteras and has a fairly realistic mean path and temporal evolution  
829 downstream, while in numerous earlier GCM simulations the Gulf Stream only separated further up the East Coast,  
830 off Long Island. Near the separation point of Chao et al.'s simulation there is a strong anticyclonic cell and northeast

831 of it a deep trough, whose axis lies at about  $69^\circ\text{W}$ . Such a trough is also present, although somewhat less pronounced,  
832 in [61] satellite observations of the Gulf Stream path at  $68^\circ\text{W}$ . The radius of the anticyclonic cell in Chao et al.'s GCM  
833 results is about 200 km, and the jet flow east of this cell is much weaker than to the west of it. From the deep trough in-  
834 tense cyclonic eddies form; these eddies propagate westward and interact with the mean jet near the separation point.

835 We interpret this ocean GCM result as follows: the anticyclonic eddy and the cyclonic trough correspond to the  
836 dipole found in all our model results. The flow's being stronger to the west of the recirculation cell and weaker to the  
837 east of it is consistent with the dipole description above. The deep trough is the cyclonic cell which wraps around the  
838 anticyclonic cell, in agreement with the average of the states shown in Fig. 5b. Intensive cyclonic eddy formation is  
839 also observed in Fig. 5b, while the eddies' westward propagation and their interaction with the mean jet are apparent  
840 in our QG simulation for later times (not shown here, but see Section 4 of [24]). The radius of the anticyclonic cell  
841 in the GCM is similar to the radius of the recirculating dipole in our numerical simulations and analytical solutions.

842 So far the good news. On the face of it, however, there are also some not-so-good news. Indeed, Greatbatch  
843 [38]—as mentioned already at the beginning of Section 5—carried out a direct comparison between the analytic  
844 “free-mode” solutions available at that time and the eddy-resolving simulations of Holland and Schmitz [55] and  
845 Böning [54]. He found a reasonably good match between their GCM results and the analytical solutions as long as the  
846 simulations reached steady state, but not when they were, in fact, fully turbulent. In the latter case, the recirculation  
847 zone's east–west extent exceeded considerably its north–south extent, while the ratio between the two was nearly  
848 unity in the steady-state solutions. Discrepancies between characteristic flow patterns at high Reynolds number  
849 and at lower Reynolds number were also pointed out in a 1.5- and 2-layer QG model with horizontal resolution  
850 comparable to the present one by Berloff and McWilliams [31].

851 We emphasize again, as done already in Section 5, that all our comparisons were carried out for the steady-state  
852 solutions of our QG and primitive-equation models, both antisymmetric and asymmetric. It was noticed that—as the  
853 wind stress increases and the intensity of the recirculation with it—the negative proportionality constant  $\alpha$  between  
854 PV and streamfunction decreases rapidly in absolute value. We expect it to be still nonzero for the periodic solutions  
855 but very close to zero for the chaotic ones, throughout the recirculation zone.

856 It is thus already the large-scale flow, in the absence of vigorous small-eddy activity, that tends to “homogenize”  
857 PV to zero in the recirculation zone. The onset of the latter eddy activity—as the Reynolds number increases—  
858 occurs therewith on a favorable background, where the spatial PV gradients, as well as the PV itself, are fairly small.  
859 This situation greatly facilitates the work of the eddies that complete the homogenization by lateral PV diffusion.

860 We note, as a concluding remark, that the relative importance of the mainly barotropic large scales vs. the mainly  
861 baroclinic smaller scales in atmospheric regime changes is a matter of active debate [62]. It is quite possible that both  
862 larger and smaller scales of motion, baroclinic as well as barotropic, might play an important role in understanding  
863 the mid-latitude oceans' low-frequency variability. To explore this issue further, a full hierarchy of ocean models—  
864 from the relatively simple ones studied here to full ocean GCMs—will be required, see [63] for applications of this  
865 approach to other fluid-dynamical problems, including the oceans' thermohaline circulation.

## 866 Acknowledgements

867 It is a pleasure to thank our collaborators in studying the double-gyre problem—K.-I. Chang, H. Dijkstra, K.  
868 Ide, G. Loeper, Z. Pan, S. Speich, E. Simonnet, R. Temam and S. Wang—for many interesting discussions. P.  
869 Berloff, H. Dijkstra and F. Primeau also provided preprints of their related work, and M. Kimoto, G. Reznik and Z.  
870 Kizner provided references. E. Simonnet read carefully an earlier version of the paper and corrected an algebraic  
871 error in deriving the analytic solution. Two anonymous referees provided constructive criticism. F. Fleuriau helped  
872 enthusiastically and patiently through many iterations of the text, and Y. Tian with the figures. This work was

873 supported by an NSF Special Creativity Award (MG), by discretionary funds of the Institute of Geophysics and  
874 Planetary Physics (IGPP) at UCLA (YF), and by NSF grant ATM-0081321 (LUS). This is IGPP publication no. 5735.

875 **Appendix A. Derivation of analytic solutions**

876 Using the spherical coordinates (21), Eq. (20) becomes

$$878 \frac{\partial^2 \psi}{\partial r^2} + \frac{2 + \delta/\eta}{r} \frac{\partial \psi}{\partial r} + \frac{1}{r^2 \sin^2 \theta} \frac{\partial^2 \psi}{\partial \varphi^2} + \frac{1}{r^2} \frac{\partial^2 \psi}{\partial \theta^2} + \frac{1}{r^2} \frac{\partial \psi}{\partial \theta} \left( \cot \theta - \frac{\delta}{\eta} \tan \theta \right) - \alpha \psi = -\beta r \sin \theta \sin \varphi. \quad (\text{A.1})$$

879 A particular solution  $\psi_{(p)} = \psi_{(p)}(r, \theta, \varphi)$  of (20) and (A.1) is

$$880 \psi = \frac{\beta}{\alpha} y = \frac{\beta}{\alpha} r \sin \theta \sin \varphi. \quad (\text{A.2})$$

881 A solution  $\psi_{(h)}$  to the homogeneous equation is obtained by separating the variables:  $\psi_{(h)} = f(r) \sin \theta \sin \varphi$ .  
882 After substituting this solution into (A.1), we obtain with some mathematical manipulation:

$$883 r^2 \frac{\partial^2 f}{\partial r^2} + \left( 2 + \frac{\delta}{\eta} \right) r \frac{\partial f}{\partial r} - \left( \alpha r^2 + 2 + \frac{\delta}{\eta} \right) f = 0. \quad (\text{A.3})$$

884 The solution to this equation depends on the sign of  $\alpha$  and can be found in [52, p. 362, Eq. (9.1.53)].

885 An anonymous reviewer pointed out that a broader class of homogeneous solutions to (A.1) can be found in terms  
886 of hyper-geometric functions  $F(a, b; c; z)$ , where  $a$  depends on  $\nu$ ,  $b$  on  $\eta$ ,  $\delta$  and  $\nu$ ,  $c$  on  $\eta$  and  $\delta$ , while  $z = \cos^2 \theta$   
887 [64]; see also Eq. (21). We would have liked to pursue this interesting hint, but feel that the qualitative fit between  
888 the surface patterns of the particular analytic solutions we have obtained and the numerical ones is rather striking  
889 and that functions with a different set of nodal lines could hardly improve upon it.

890 In the recirculating region we obtain

$$891 r < r_0, \quad \alpha = -k^2 < 0, \quad f(kr) = \frac{J_\nu(kr)}{r^{\nu-1}}, \quad (\text{A.4a})$$

892 while in the exterior region:

$$893 r > r_0, \quad \alpha = p^2 > 0, \quad f(pr) = \frac{K_\nu(pr)}{r^{\nu-1}}. \quad (\text{A.4b})$$

894 Here  $J_\nu$  and  $K_\nu$  are Bessel and modified Bessel functions of order  $\nu = (3 + \delta/\eta)/2$  and the first kind, with  $\nu \geq 3/2$   
895 according to Eq. (23).

896 If  $\psi \neq 0$  on  $r = r_0$ , the absolute vorticity  $Q$  is discontinuous, given the discontinuity of  $\alpha$  in Eq. (20); thus  
897  $r = r_0$  must be a streamline. If  $\psi = 0$  on  $r = r_0$ , however, then the vorticity  $Q$  can be continuous—since  $Q = 0$   
898 there as well, according to Eq. (20)—provided

$$899 A = \frac{\beta r_0^\nu}{k^2 J_\nu(kr_0)}, \quad B = \frac{\beta r_0^\nu}{p^2 K_\nu(pr_0)}. \quad (\text{A.5})$$

900 In this case, Eqs. (22a) and (22b) can be written as follows:

$$901 \psi = \frac{\beta r_0}{k^2} \left[ \left( \frac{kr_0}{kr} \right)^{\nu-1} \frac{J_\nu(kr)}{J_\nu(kr_0)} - \frac{r}{r_0} \right] \sin \theta \sin \varphi, \quad r < r_0, \quad (\text{A.6a})$$

$$902 \psi = \frac{\beta r_0}{p^2} \left[ - \left( \frac{pr_0}{pr} \right)^{\nu-1} \frac{K_\nu(pr)}{K_\nu(pr_0)} + \frac{r}{r_0} \right] \sin \theta \sin \varphi, \quad r > r_0. \quad (\text{A.6b})$$

903 For the velocity to be continuous on  $r = r_0$ ,  $\partial\psi/\partial r$  must be continuous there, too. Using the identities

$$904 \quad J'_v(kr) = \frac{vJ_v(kr)}{r} - kJ_{v+1}(kr), \quad K'_v(pr) = \frac{vK_v(pr)}{r} - pK_{v+1}(pr), \quad (\text{A.7})$$

905 we obtain the following condition for the latter to hold:

$$906 \quad -\frac{1}{kr_0} \left[ \frac{J_{v+1}(kr_0)}{J_v(kr_0)} \right] = \frac{1}{pr_0} \left[ \frac{K_{v+1}(pr_0)}{K_v(pr_0)} \right]. \quad (\text{A.8})$$

907 Here the parameters  $-k^2$  and  $p^2$  are the coefficients of proportionality between  $Q$  and  $\psi$  inside and outside the  
 908 dipole, respectively. For  $0 < pr_0 < \infty$ , the condition (A.8) yields a range  $(a, b)$  for  $kr_0$ , given by (24). This  
 909 completes the derivation of the antisymmetric solution.

910 The continuity conditions on the rider  $\psi_R$  are used next to determine the constants  $A$ ,  $B$  and  $D$  in Eqs. (30a) and  
 911 (30b). The rider  $\psi_R$  has a streamline on  $r = r_0$  and has to be continuous there, so that

$$912 \quad A \frac{J_\omega(kr_0)}{r_0^\omega} + D = B \frac{K_\omega(pr_0)}{r_0^\omega}. \quad (\text{A.9})$$

913 The continuity of the velocity on  $r_0$  is obtained when  $\partial\psi_R/\partial r$  is continuous there. After some mathematical  
 914 manipulation, using the identities (A.7), we obtain the following relationship:

$$915 \quad B = -A \left( \frac{kr_0}{pr_0} \right) \frac{J_{\omega+1}(kr_0)}{K_{\omega+1}(pr_0)}, \quad (\text{A.10})$$

916 and from (A.9) we get

$$917 \quad D = -\frac{A}{r_0^\omega} \left[ J_{\omega+1}(kr_0) \frac{K_\omega(pr_0)kr_0}{K_{\omega+1}(pr_0)pr_0} + J_\omega(kr_0) \right]. \quad (\text{A.11})$$

918 This completes the derivation of the symmetric free mode.

919 The appearance of oscillatory Bessel functions in our complete analytic solutions presents an additional interest.  
 920 Berloff and Meacham [19] and Primeau [65] found a variable number of meanders in the downstream direction  
 921 for a single- and double-gyre barotropic model's equilibria, respectively. It is tempting, at least, to attribute this  
 922 increasing number of meanders, and of possible equilibria associated with them, to the Bessel functions that can be  
 923 "fitted" in the zonal direction within a rectangular basin of given size. To clarify further this connection requires  
 924 matching our analytic modon solutions, strictly valid in the D region only, to Fofonoff-type solutions valid in the G  
 925 region.

## 926 References

- 927 [1] H. Stommel, The westward intensification of wind-driven current, *Trans. Am. Geophys. Union* 29 (1948) 202–206.  
 928 [2] W.H. Munk, On the wind-driven ocean circulation, *J. Meteorol.* 7 (1950) 79–93.  
 929 [3] N.P. Fofonoff, Steady flow in a frictionless homogeneous ocean, *J. Mar. Res.* 13 (1954) 254–262.  
 930 [4] G. Veronis, An analysis of wind-driven ocean circulation with a limited number of Fourier components, *J. Atmos. Sci.* 20 (1963) 557–593.  
 931 [5] G. Veronis, Wind-driven ocean circulation. Part II: Numerical solution of the nonlinear problem, *Deep-Sea Res.* 13 (1966) 31–55.  
 932 [6] J. Pedlosky, *Geophysical Fluid Dynamics*, 2nd Edition, Springer, Berlin, 1987.  
 933 [7] J. Pedlosky, *Ocean Circulation Theory*, Springer, Berlin, 1996.  
 934 [8] Climate Research Committee, *Global Ocean–Atmosphere–Land System (GOALS) for Predicting Seasonal-to-Interannual Climate*, National  
 935 Academy Press, Washington, DC, 1994.  
 936 [9] D. Martinson, K. Bryan, M. Ghil, M. Hall, T. Karl, E. Sarachik, S. Sorooshian, L. Talley (Eds.), *Natural Climate Variability on  
 937 Decade-to-Century Time Scales*, National Academy Press, Washington, DC, 1995.

- 938 [10] S. Jiang, F.F. Jin, M. Ghil, The nonlinear behavior of western boundary currents in a wind-driven, double-gyre, shallow-water model, in:  
939 Preprints of the Ninth Conference on Atmospheric, Oceanic Waves and Stability, American Meteorological Society, Boston, MA, 1993,  
940 pp. 64–67.
- 941 [11] S. Jiang, F.F. Jin, M. Ghil, Multiple equilibria, periodic and aperiodic solutions in a wind-driven, double gyre, shallow-water model, *J.*  
942 *Phys. Oceanogr.* 25 (1995) 764–786.
- 943 [12] P. Cessi, G.R. Ierley, Symmetry-breaking multiple equilibria in quasi-geostrophic, wind-driven flows, *J. Phys. Oceanogr.* 25 (1995) 1196–  
944 1205.
- 945 [13] M. Ghil, S. Childress, *Topics in Geophysical Fluid Dynamics: Atmospheric Dynamics, Dynamo Theory and Climate Dynamics*, Springer,  
946 New York, 1987.
- 947 [14] S. Speich, H. Dijkstra, M. Ghil, Successive bifurcations in a shallow-water model applied to the wind-driven ocean circulation, *Nonlinear*  
948 *Proc. Geophys.* 2 (1995) 241–268.
- 949 [15] J. McCalpin, D.B. Haidvogel, Phenomenology of the low-frequency variability in a reduced-gravity, quasigeostrophic double-gyre model,  
950 *J. Phys. Oceanogr.* 26 (1996) 739–752.
- 951 [16] B. Moro, On the non-linear Munk model. I: Steady flows, *Dyn. Atmos. Oceans* 12 (1988) 259–288.
- 952 [17] B. Moro, On the non-linear Munk model. II: Steady flows, *Dyn. Atmos. Oceans* 14 (1990) 203–237.
- 953 [18] H.A. Dijkstra, C.A. Katsman, Temporal variability of the wind-driven quasi-geostrophic double gyre ocean circulation: basic bifurcation  
954 diagrams, *Geophys. Astrophys. Fluid Dyn.* 85 (1997) 195–232.
- 955 [19] P. Berloff, S.P. Meacham, The dynamics of an equivalent-barotropic model of the wind-driven circulation, *J. Mar. Res.* 55 (1997) 407–451.
- 956 [20] P. Berloff, S.P. Meacham, The dynamics of a simple baroclinic model of the wind-driven circulation, *J. Phys. Oceanogr.* 28 (1998) 361–388.
- 957 [21] G.R. Flierl, Models of vertical structure and the calibration of two-layer models, *Dyn. Atmos. Oceans* 2 (1978) 341–381.
- 958 [22] Y. Feliks, Isolated vortex evolution in 2 and 4 mode models, *Deep-Sea Res.* 37 (1990) 571–591.
- 959 [23] Y. Feliks, M. Ghil, Downwelling-front instability and eddy formation in the Eastern Mediterranean, *J. Phys. Oceanogr.* 23 (1993) 61–78.
- 960 [24] Y. Feliks, M. Ghil, Mixed barotropic–baroclinic eddies growing on an eastward midlatitude jet, *Geophys. Astrophys. Fluid Dyn.* 82 (1996)  
961 137–171.
- 962 [25] K.I. Chang, M. Ghil, K. Ide, C.A. Lai, Transition to aperiodic variability in a wind-driven double-gyre circulation model, *J. Phys. Oceanogr.*  
963 31 (2001) 1260–1286.
- 964 [26] P.L. Richardson, Gulf Stream rings, in: A.R. Robinson (Ed.), *Eddies in Marine Science*, Springer, Berlin, 1983.
- 965 [27] D.B. Haidvogel, A.R. Robinson, E.E. Schulman, The accuracy, efficiency and stability of three numerical models with application to open  
966 ocean problems, *J. Comput. Phys.* 34 (1980) 1–53.
- 967 [28] R. Shapiro, Smoothing, filtering, and boundary effects, *Rev. Geophys. Space Phys.* 8 (1970) 359–387.
- 968 [29] D. Marshall, J. Marshall, Zonal penetration scale of midlatitude oceanic jets, *J. Phys. Oceanogr.* 22 (1992) 1018–1032.
- 969 [30] G.L. Barenblatt, *Dimensional Analysis*, Gordon and Breach, New York, 1987.
- 970 [31] P. Berloff, J.C. McWilliams, Large-scale, low-frequency variability in wind-driven ocean gyres, *J. Phys. Oceanogr.* 29 (1999) 1925–1949.
- 971 [32] E. Simonnet, M. Ghil, K. Ide, R. Temam, S. Wang, Low-frequency variability in shallow-water models of the wind-driven ocean circulation.  
972 Part I: Steady-state solutions, *J. Phys. Oceanogr.*, submitted for publication.
- 973 [33] E. Simonnet, M. Ghil, K. Ide, R. Temam, S. Wang, Low-frequency variability in shallow-water models of the wind-driven ocean circulation.  
974 Part II: Time-dependent solutions, *J. Phys. Oceanogr.*, submitted for publication.
- 975 [34] H. Goldstein, *Classical Mechanics*, Addison-Wesley, Reading, MA, 1980.
- 976 [35] J.C. McWilliams, G.R. Flierl, On the evolution of isolated, nonlinear vortices, *J. Phys. Oceanogr.* 9 (1979) 1155–1182.
- 977 [36] P. Cessi, G. Ierley, W. Young, Model of the inertial recirculation driven by potential vorticity anomalies, *J. Phys. Oceanogr.* 17 (1987)  
978 1640–1652.
- 979 [37] R.J. Greatbatch, A model for the inertial recirculation of a gyre, *J. Mar. Res.* 45 (1987) 601–634.
- 980 [38] R.J. Greatbatch, On the scaling of inertial subgyres, *Dyn. Atmos. Oceans* 11 (1988) 265–285.
- 981 [39] M.E. Stern, Minimal properties of planetary eddies, *J. Mar. Res.* 33 (1975) 1–33.
- 982 [40] V.D. Larichev, G.M. Reznik, Two-dimensional solitary Rossby waves, *Rep. USSR Acad. Sci.* 231 (1976) 1077–1080.
- 983 [41] G.W. Branstator, J.D. Opsteegh, Free solutions of the barotropic vorticity equation, *J. Atmos. Sci.* 46 (1989) 1799–1814.
- 984 [42] J. Marshall, D.W.K. So, Thermal equilibration of planetary waves, *J. Atmos. Sci.* 47 (1990) 963–978.
- 985 [43] R.T. Pierrehumbert, P. Malguzzi, Forced coherent structures and local multiple equilibrium in a barotropic atmosphere, *J. Atmos. Sci.* 41  
986 (1984) 246–257.
- 987 [44] G. Wolansky, Existence, uniqueness, and stability of stationary barotropic flow with forcing and dissipation, *Commun. Pure Appl. Math.*  
988 41 (1988) 19–46.
- 989 [45] G. Wolansky, The barotropic vorticity equation under forcing and dissipation bifurcations of nonsymmetric responses and multiplicity of  
990 solutions, *SIAM J. Appl. Math.* 49 (1989) 1585–1607.
- 991 [46] F.P. Bretherton, D.B. Haidvogel, Two-dimensional turbulence above topography, *J. Fluid Mech.* 78 (1976) 129–154.
- 992 [47] J. Marshall, G. Nurser, Steady, free circulation in a stratified quasi-geostrophic ocean, *J. Phys. Oceanogr.* 16 (1986) 1799–1813.
- 993 [48] Y. Feliks, On Rossby radius of deformation in the ocean, *J. Phys. Oceanogr.* 15 (1985) 1605–1607.
- 994 [49] Y. Feliks, M. Ghil, Stability of a front separating water masses with different stratifications, *Geophys. Astrophys. Fluid Dyn.* 84 (1997)  
995 165–204.

- 996 [50] A.L. Berestov, Solitary Rossby waves, *Izv. Akad. Nauk SSSR Fiz. Atmos. Okeana* 15 (1979) 648–654.
- 997 [51] H. Sakuma, M. Ghil, Stability of propagating modons for small-amplitude perturbations, *Phys. Fluids A* 3 (1991) 408–414.
- 998 [52] M. Abramowitz, I.A. Stegun, *Handbook of Mathematical Functions*, National Bureau of Standards, 1964.
- 999 [53] Z.I. Kizner, Theory of eddies in the thermocline, *Dokl. Akad. Nauk SSSR* 300 (1987) 213–216.
- 1000 [54] C. Böning, On the influence of frictional parameterization in wind-driven ocean circulation models, *Dyn. Atmos. Oceans* 10 (1986) 63–92.
- 1001 [55] W.R. Holland, W.J. Schmitz, Zonal penetration scale of model midlatitude jets, *J. Phys. Oceanogr.* 15 (1985) 1859–1875.
- 1002 [56] P.B. Rhines, W.R. Young, Homogenization of potential vorticity in planetary gyres, *J. Fluid Mech.* 122 (1982) 347–367.
- 1003 [57] S. Jiang, Data assimilation for a nonlinear, wind-driven, shallow-water model in a rectangular midlatitude basin, Ph.D. Thesis, University  
1004 of California, Los Angeles, CA, 1994.
- 1005 [58] S. Jiang, M. Ghil, Tracking nonlinear solutions with simulated altimetric data in a shallow-water model, *J. Phys. Oceanogr.* 27 (1997)  
1006 72–95.
- 1007 [59] R. Salmon, Hamiltonian fluid mechanics, *Ann. Rev. Fluid Mech.* 20 (1988) 225–256.
- 1008 [60] Y. Chao, A. Gangopadhyay, F.O. Bryan, W.R. Holland, Modelling the Gulf Stream system: how far from reality? *Geophys. Res. Lett.* 23  
1009 (1996) 3155–3158.
- 1010 [61] T. Lee, P. Cornillon, Propagation and growth rate of Gulf Stream meanders between 75° and 45°W, *J. Phys. Oceanogr.* 26 (1996) 225–241.
- 1011 [62] G.W. Branstator, Organization of storm track anomalies by recurring low-frequency circulation anomalies, *J. Atmos. Sci.* 52 (1995) 207–226.
- 1012 [63] M. Ghil, A.W. Robertson, Solving problems with GCMs: general circulation models and their role in the climate modeling hierarchy, in:  
1013 D. Randall (Ed.), *General Circulation Model Development: Part, Present and Future*, Academic Press, San Diego, CA, 1999, pp. 285–325.
- 1014 [64] W. Magnus, F. Oberhettinger, R.P. Soni, *Formulas and Theorems for the Special Functions of Mathematical Physics*, Springer, Berlin,  
1015 1966.
- 1016 [65] F.W. Primeau, Multiple equilibria of a double-gyre ocean model with super-slip boundary conditions, *J. Phys. Oceanogr.* 28, 2130–2147.